Title

Investigating protein-membrane relationships at the atomistic level using computational approaches

Author

Gomez, Yessica Kassandra

Publication Date

2023

Investigating protein-membrane relationships at the atomistic level using computational approaches

by
Yessica Kassandra Gomez

DISSERTATION
Submitted in partial satisfaction of the requirements for degree of
DOCTOR OF PHILOSOPHY

in

Biophysics

in the

GRADUATE DIVISION
of the
UNIVERSITY OF CALIFORNIA, SAN FRANCISCO

Approved:

DocuSigned by:
Michael Grabe
5B8B990D587B414...

Michael Grabe
Chair

DocuSigned by:
William DeGrado
[illegible]...

William DeGrado

DocuSigned by:
Lily Jan
394456D87457494...

Lily Jan

Committee Members

Acknowledgements

This work was accomplished with the support, both personal and professional, of many people.

I had a great training experience in the Grabe lab, and I especially want to credit Frank, Paola, Andrew, Christina, Jamie, and (of course) Michael for their advice, support, feedback, and collaboration. I'm so glad none of you fell in the ocean at our last lab retreat.

I am grateful to my thesis committee and our various collaborators because I have learned so much (about membrane proteins) through our work together. My gratitude goes to Bill DeGrado and Lily Jan; to Jeff Brodsky and Chris Guerriero at Pitt; to Jeff Abramson, Farha Khan, and Lucie Bergdoll (formerly) from UCLA; and to Rob Edwards, Bob Stroud, Fei Li, Jacob Eriksen, and everyone else working on VGLUT2.

Many thanks to my grad school friends and roommates for the game nights, hikes, dinners, laughs, commiseration, and companionship. Chris, Snow, Christina, Luca, Andrew (again), Keely, Sophia, Matan, Daniel, and Wren – if you're reading this, thank you for actually looking at my dissertation.

Finally, thank you to my family. To my husband, Matvei: thank you for the places we've seen, the people we've met, and the life we've built together. To Gael: thank you for your unwavering belief in me and for being unapologetically yourself. And to my mom and dad: ustedes saben que sin ti nada de esto fuera posible. Se les agradece, hoy y siempre. This work is dedicated to them.

Contributions

Chapter 2 has been adapted from a previously published journal article:

Gomez, Y. K.*; Natale, A. M.*; Lincoff, J.*; Wolgemuth, C. W.; Rosenberg, J. M.; Grabe, M. Taking the Monte-Carlo Gamble: How Not to Buckle under the Pressure! J Comput Chem 2021, jcc.26798. https://doi.org/10.1002/jcc.26798.

*Equal contribution

Chapter 3 has been adapted from a previously published journal article:

Guerriero, C. J.; Gomez, Y. K.; Daskivich, G. J.; Reutter, K.-R.; Augustine, A. A.; Weiberth, K. F.; Nakatsukasa, K.; Grabe, M.; Brodsky, J. L. Harmonizing Experimental Data with Modeling to Predict Membrane Protein Insertion in Yeast. Biophysical Journal 2019, 117 (4), 668–678. https://doi.org/10.1016/j.bpj.2019.07.013.

Chapter 4 has been adapted from a manuscript in preparation for submission. Co-authors on this work include Frank V. Marcoline, Charles W. Wolgemuth, and Michael Grabe.

Investigating protein-membrane relationships at the atomistic level using computational approaches

Yessica Kassandra Gomez

Abstract

In this work, I will discuss the insight we can gain into biophysical processes by looking at atomistic details using computational methods. The focus will be on describing protein-membrane interactions using molecular dynamics simulations and continuum models. I will begin with the ongoing improvements being made to molecular dynamics simulations; specifically, one contribution made to improve a popular pressure-maintenance algorithm known as a barostat. I will then discuss two cases that employ the molecular dynamics combined with continuum modeling approach to fruitful ends. The first shows how a physics-based scale of protein insertion free energy applied to a model system comprising a dual-pass transmembrane helix reporter fused to a misfolded domain yielded membrane insertion predictions that were more accurate than existing bioinformatics approaches. Follow-up molecular dynamics simulations suggested that cases with unexpectedly high insertion resulted from stabilizing hydrogen bonds, emphasizing the need for further investigation of the properties that influence transmembrane helix insertion. The second case attempts to reconcile existing mechanosensation models with emerging data about the mechanosensitive channel of small conductance by comparing the open and closed states with molecular dynamics simulations, then constructing a continuum elasticity model to reproduce the dramatic membrane behavior. A quantitative analysis of this model highlights the importance of tension in membrane free energy and offers suggestions for bridging the apparent gap between the ‘force-from-lipids’ paradigm and the newer ‘membrane deformation’ model.

Table of Contents

List of Figures

List of Tables

List of Abbreviations

ABC - ATP-binding Cassette

APL - Area-Per-Lipid

APBS - Adaptive Poisson-Boltzmann Solver

BCs - Boundary conditions

BHK - Baby Hamster Kidney (cell line)

BNID - BioNumbers 6-digit identifier

C36 - CHARMM36

CFTR - Cystic Fibrosis Transmembrane Conductance Regulator

CGMD - Coarse-Grain Molecular Dynamics

CHX - Cycloheximide

EDTA - Ethylenediaminetetraacetic Acid

Endo H - Endoglycosidase H

ER - Endoplasmic Reticulum

ERAD - ER-associated Degradation

FS - Force-Switching

HA - Hemagglutinin

HRP - Anti-HA-Horseradish Peroxidase

LJ - Lennard–Jones

L17 - Lipid17

MC - Monte-Carlo

MD - Molecular Dynamics

MscL - Mechanosensitive channel of large conductance

MscS - Mechanosensitive channel of small conductance

NBD - Nucleotide-Binding Domain

PCR - Polymerase Chain Reaction

PGK - Phosphoglycerate Kinase

SDS-PAGE - Sodium Dodecyl Sulfate–Polyacrylamide Gel Electrophoresis

TCA - Trichloroacetic Acid

TMH - Transmembrane Helix

VDW - Van-der-Waals

1. INTRODUCTION

Nearly thirty percent of proteins reside in a biomembrane (BNID 106431) (Milo et al.), where they carry out signaling, sensing, and transport functions. During these processes, the membrane is not static; rather, it has dynamic chemical and physical interactions with the proteins that influences both structure and function. A prime example is hydrophobic mismatch, where the nonpolar regions of a membrane and a protein do not align. This (missed) connection between protein structure and lipid thickness or composition is powerful enough to drive protein insertion, trafficking, and conformational changes. As for function, many classes of proteins have evolved to carry out membrane-dependent tasks, such as: lipid scramblases which modulate the composition of different membrane leaflets, ion channels which control the salt concentrations on both sides of the bilayer, small molecule transporters, and mechanosensitive proteins that respond to forces in the membrane. Without proteins like these, cellular life would not be possible, and today they make up over 50% of pharmaceutical targets (Overington et al.). To better understand the behavior of these key molecules it is necessary to investigate their complex relationships with the membrane.

One way to probe the protein-membrane relationship is with computational models, particularly physics-based techniques that provide a high level of atomic detail. Such techniques can give information about kinetics and thermodynamic properties such as free energies and equilibrium configurations. The focus of this work will be on the application of several such techniques to questions of membrane protein biology; relevant techniques are outlined below.

Molecular dynamics simulation

Molecular dynamics simulation (MD) is a computational method that generates detailed physical predictions of a system over time. Classical MD in biology refers to a fully atomistic representation of a system containing a biomolecule, solvent, and optionally a membrane. This system, wherein atoms are treated as charged spheres connected by springs representing chemical bonds, is subjected to Van-der-

Waals (VDW) and electrostatic forces at set time intervals known as timesteps. The forces are determined by the nature and distance of the surrounding particles, using predetermined sets of interaction values called force-fields. Many force-fields exist which attempt to replicate experimentally observed interactions and improvement of force-fields is an ongoing area of development. Given that a typical simulation system contains upwards of tens of thousands of atoms however, calculating the force between all pairs of molecules in a system at every timestep is not tractable. For this reason, it is useful to define a radius around the atom within which all neighbor interactions are calculated and beyond which a constant value is applied, known as a cut-off distance. Alternatively, a force-switching scheme can be used to smoothly taper the forces to zero over a radial range. All simulation systems exist in a faux-infinite matrix called periodic boundary conditions, wherein the system is surrounded on all sides by copies of itself thereby preventing the edges of the system from experiencing a vacuum.

While MD can be a powerful tool, it is also in an ongoing state of refinement to better represent experimentally derived properties of molecules. Chapter 1 highlights one instance of correcting a problem in a popular MD protocol to ensure simulated membrane properties match experimental values (Gomez et al.). Specifically, while the Monte Carlo (MC) barostat (Åqvist et al.) has become a common choice for maintaining constant pressure conditions in a simulation due to its improved ability to model the correct statistical ensemble, it needs improvement. When using MC barostat in combination with hard cut-off distances, rather than a force-switching scheme, highly unphysical membrane behavior was observed in large membrane systems. This parameter choice is common, but the adverse consequences had not been reported until very recently as the effects are smaller in membrane patches of typical size. The problem arises because of a mismatch in the handling of potentials and forces in the dynamical equations versus the MC barostat, but it can be avoided by employing a force-switching scheme even with very small ΔD. Greater detail, as well as a mathematical description of this behavior, is provided in Chapter 1.

MD can be computationally expensive, and a variety of methods exist to speed up simulation times depending on the properties of interest. One popular approach is coarse-grain MD (CGMD), where spheres represent larger units such as functional groups of atoms or even peptides. A popular CGMD

representation is the MARTINI model (Marrink et al.) that uses a 4-to-1 mapping, where single beads represent groups of four heavy atoms and their associated hydrogens. This method is employed in Chapter 3 to collect tens of microseconds of data to determine the shape of the membrane around a mechano-sensing protein at equilibrium. While some physical detail is lost, comparison to prior work shows that this model produces the same membrane behavior as the corresponding atomistic simulations.

Continuum models

While a detailed physical picture over the nanosecond to microsecond timescale provides a high level of atomic detail, it can also require long wall clock times to sample events of biological interest such as membrane partitioning and binding of small molecules to proteins, which often happen on the order of milliseconds, particularly if no enhancement or steering methods are used. Because of this, it can be difficult to measure equilibrium properties of phenomena such as deformation of membranes by proteins or free energy of partition into a membrane for large molecules. In these instances, it is much more efficient to use a simplified representation, such as a continuum model, to quickly calculate these properties of interest. In particular, continuum elasticity theory is well suited for fast, physical considerations of protein-membrane interactions.

The Grabe lab has introduced a hybrid continuum-atomistic model which can quantitatively predict, among other things, free energy of protein insertion into membranes and membrane deformations around proteins (Marcoline et al.; Argudo, Bethel, Marcoline, and Grabe). It performs as well as MD but requires orders of magnitude less computational time. Previous predictions arising from the model include an early description of extreme membrane bending around the hydrophilic groove of the nhTMEM16 scramblase (Bethel and Grabe), which was subsequently validated by structures solved using cryogenic electron microscopy (Kalienkova et al.). Another such application involves a model system containing two anchor helices and a misfolded domain developed to probe endoplasmic reticulum associated degradation (ERAD) in yeast. Point mutations in one of the anchor helices were made, resulting in free energy and conformational changes that directly affected insertion probability. This information was then used to

carry out targeted MD simulations which provided insight into the determinants of peptide insertion in the membrane (Guerriero, Gomez, et al.). A detailed discussion of this system is found in Chapter 2.

This method can also be used to expand existing models of mechanosensation. Mechanosensitive membrane proteins are those that can convert tension in the membrane into area expansion either directly or with the involvement of the cytoskeleton or accessory proteins. The proteins that accomplish this directly using force-from-lipids could do so in a variety of ways, either by retaining lipid contacts (dragging model), losing lipid contacts (entropy model), or protein curvature (membrane dome model) (Kefauver et al.). However, it is possible that instead of sensing tension through direct lipid interactions, they may sense tension through changes in bulk membrane properties such as shear stress, area expansion or curvature. In particular, the mechanosensitive channel of small conductance (MscS) was initially thought to function like its bacterial neighbor the mechanosensitive channel of large conductance (MscL), which responds to force by opening like a camera shutter and increasing its surface area, possibly by direct interaction between an amphipathic helix and a nearby lipid (Perozo, Cortes, et al.; Kefauver et al.). However, this similarity has been disputed since the emergence of very different crystal structures for each. Recent structural and computational work by Park and others has proposed that MscS channel opening is driven by large deformations of the membrane around the protein in the closed state and shows no change in the in-plane surface area between open and closed states (Park et al.). Chapter 3 describes the efforts thus far to reconcile this emerging model of mechanosensation with existing ideas about the role of area expansion, tension and hydrophobic mismatch in mechanosensation (Wiggins and Phillips). This latest continuum model approach, in combination with MD simulation, seeks to provide an updated physical description for tension sensing through membrane curvature.

In summary, computational methods like MD and continuum modeling are a powerful way to gain insight into biological processes by looking at atomic details in a way that is not possible experimentally.

2. TAKING THE MONTE-CARLO GAMBLE: HOW NOT TO BUCKLE UNDER THE PRESSURE!

Consistent buckling distortions of a large membrane patch (200 × 200 Å) are observed during molecular dynamics (MD) simulations using the Monte-Carlo (MC) barostat in combination with a hard Lennard–Jones (LJ) cutoff. The buckling behavior is independent of both the simulation engine and the force field but requires the MC barostat-hard LJ cutoff combination. Similar simulations of a smaller patch (90 × 90 Å) do not show buckling, but do show a small, systematic reduction in the surface area accompanied by ~1 Å thickening suggestive of compression. We show that a mismatch in the way potentials and forces are handled in the dynamical equations versus the MC barostat results in a compressive load on the membrane. Moreover, a straightforward application of elasticity theory reveals that a minimal compression of the linear dimensions of the membrane, inversely proportional to the edge length, is required for buckling, explaining this differential behavior. We recommend always using LJ force or potential-switching when the MC barostat is employed to avoid undesirable membrane deformations.

Main Text

We observed consistent undesirable distortions of a membrane patch during molecular dynamics (MD) simulations in Amber18 using the Monte-Carlo (MC) barostat (Åqvist et al.) in combination with a standard 10 Å hard Lennard–Jones (LJ) cutoff as recently mentioned by Im and colleagues (Lee, Hitzenberger, et al.); here we report our successful efforts to ameliorate this problem by employing force-switching (FS). The MC barostat, which is currently implemented in Amber and OpenMM, is a relatively new barostat that is frequently used for constant pressure simulations as it reproduces the correct volume fluctuations, unlike the Berendsen barostat (Berendsen et al.), and it does not require the virial to be computed at every time step, unlike most barostats (Åqvist et al.). Meanwhile, a 9 or 10 Å hard cutoff for nonbonded interactions is commonly employed to improve simulation speed, as explicitly recommended for use with Amber force fields. When these parameters are used to simulate a 200 × 200 × 80 Å box, we observe significant rapid buckling of an initially flat membrane into an egg carton pattern that then breaks xy-symmetry to relax into a sinusoidal plane wave, as shown in Figure 2.1.

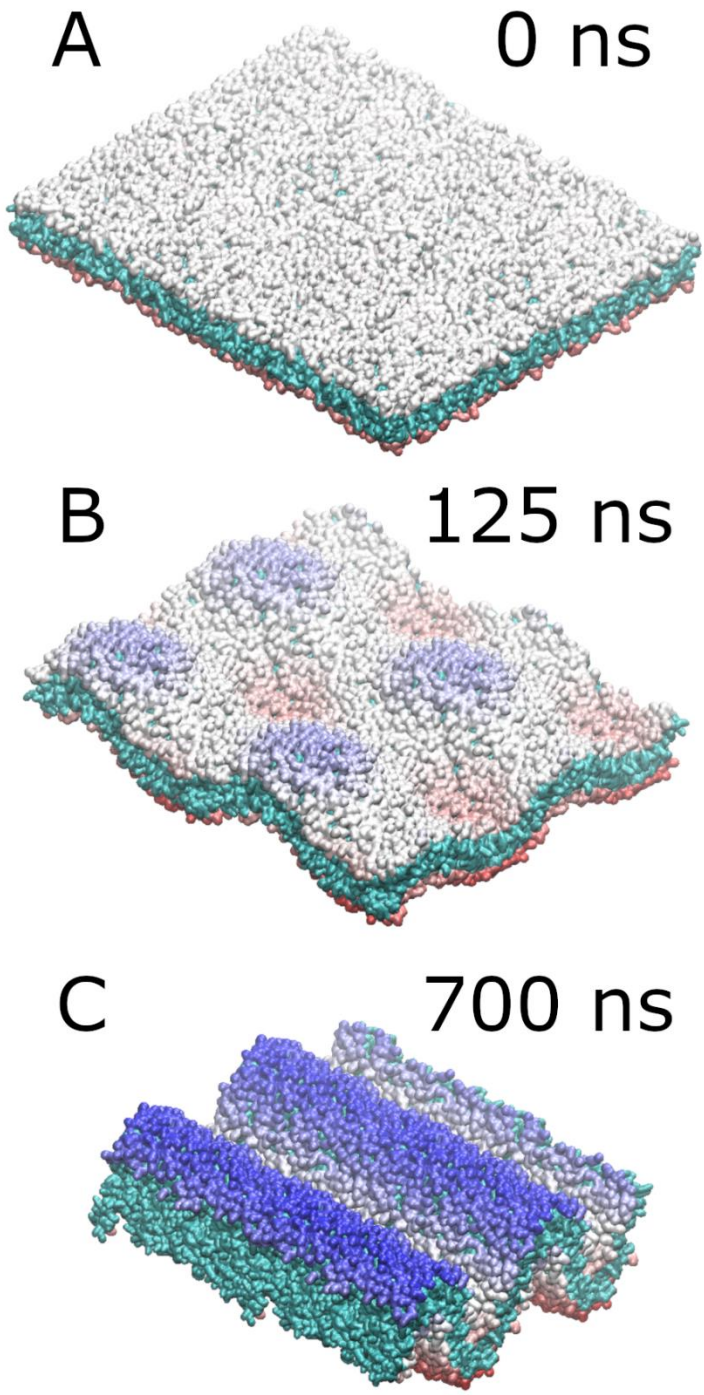

Figure 2.1 Membrane deformation induced by MC barostat and 10 Å cutoff.
A 200 x 200 Å patch of POPC membrane with the hydrophobic lipid tails colored cyan and the head groups colored by height (z-coordinate – Blue positive, red negative). Note that all three panels show a 2 x 2 array of four simulation cells. (A) The initially flat membrane at the start of production exhibits minor height fluctuations. (B) By 125 ns, the membrane has buckled into an egg carton shape (see text). (C) By 700 ns, buckling has continued into nearly a steady state shape (see text).

After this initial observation, we ran a series of test simulations using different MD engines to isolate which parameter combinations correlate with membrane distortions (Supplementary Table A1), comparing the MC algorithm with (1) the widely available but problematic, Berendsen barostat and (2) the Parrinello-Rahman barostat (Parrinello and Rahman) implementation in Gromacs, which like the MC algorithm properly samples volume fluctuations. All simulations used semi-isotropic pressure scaling with coupling in the initial plane of the membrane (x–y plane) independent of the perpendicular axis. Examination of the box dimensions over time reveals that all simulations keep a constant volume (Supplementary Figure A1), albeit with up to 3% initial variation in the first few time steps in some cases; however, the MC barostat when used in combination with a 10 Å hard cutoff always results in a gradual compression of the x–y plane, and corresponding expansion along z, on the 100-ns timescale (yellow traces in Figure 2.2A–C), leading to deformations like those shown in Figure 2.1.

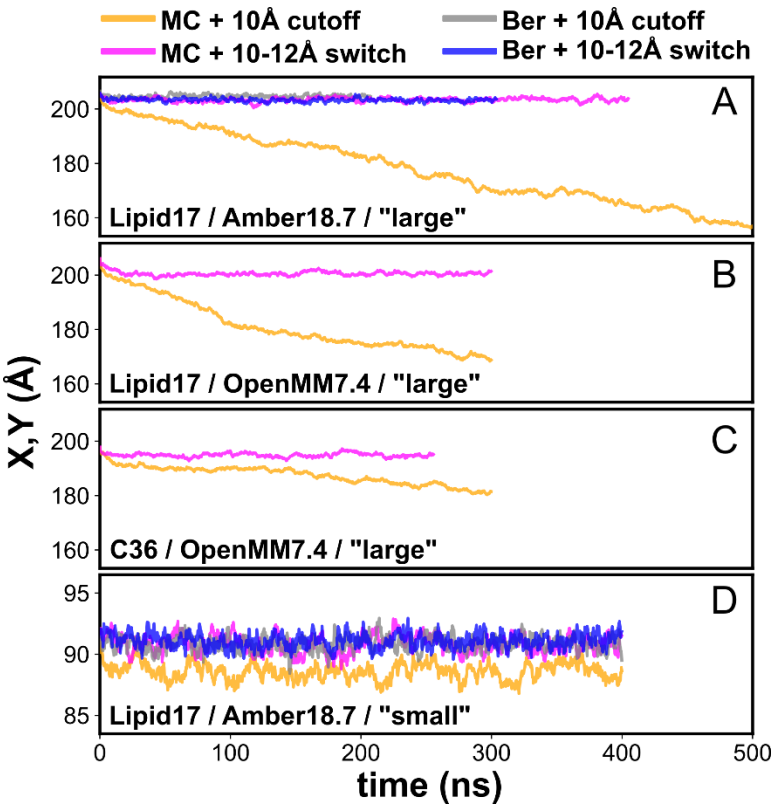

Figure 2.2 Changes in x/y-box dimensions over time for different combinations of system parameters. (Figure caption continued on the next page.)

(Figure caption continued from the previous page.) The identical length and width (x,y) of the membrane patches are plotted against time. The color key at the top defines combinations of barostats (MC-MC barostat or Ber-Berendsen) with LJ treatments (10 Å cutoff or 10–12 Å force switching). Each panel shows results for additional model combinations: (A) large membrane patch (initially 200 x 200 Å), Amber18.7 engine, and Lipid17 force field (#1-#4); (B) large patch, OpenMM7.4 engine, and Lipid17 (#9,#10); (C) large patch, OpenMM7.4 engine, and CHARMM36 force field (#11,#12); and (D) small patch (initially 90 x 90 Å), Amber18.7 engine, and Lipid17 (#15,#17,#18,#20). All numbers refer to simulations in Supplementary Information Table A1.

Importantly, this phenomenon is not an artifact of a particular MD engine or force field as the buckling is reproduced in OpenMM as well as simulations performed with CHARMM36 (Supplementary Table A1), though CHARMM force fields are explicitly recommended for use with FS only. This suggests that the origin of the problem lies with the pairing of the MC barostat and a 10 Å (or shorter) LJ cutoff in membrane simulations. No other parameter combinations in Supplementary Table A1 resulted in significant membrane deformation.

We note that most published simulations employing the MC barostat in combination with a short LJ cutoff use smaller membrane patches, and they appear to be free of the distortions described above. We therefore tested whether 90 × 90 Å bilayers undergo buckling and found that that they do not (Supplementary Table A1 and Supplementary Figure A1F). That said, the MC barostat simulation with 10 Å LJ cutoff does experience a 2 Å decrease of the x and y dimensions (yellow trace in Figure 2.2D) and a corresponding ~1 Å thickening of the width as if the membrane is under compression. Taken together, the extreme buckling observed on the large membrane patches coupled with the modest compression of the smaller patch suggests that there is an effective compressive force in the membrane plane when the semi-isotropic MC barostat is used with a hard cutoff.

Changes to the LJ parameters are known to impact atomistic properties, including the particularly sensitive lipid density. Specifically, a hard LJ truncation of 10 Å reduces long range attraction compared to, say, a 10–12 Å switching distance, and might be expected to lead to a greater area-per-lipid (APL), as it does for the Berendsen barostat simulations (#3 and #4 in Supplementary Table A1). Why then does the MC barostat compress membranes when a short hard cutoff is employed? We believe that this arises from an inconsistency between the way forces and potentials are handled in the MC trial box-size change stage

versus the dynamics stage. The MC barostat uses the potentials between pairs of atoms to determine whether a random box rescaling is energetically favorable. For a given configuration, atoms separated by a distance greater than the cutoff have zero interaction energy. However, in the dynamics steps, it is the force between atom pairs that is set to zero outside the cutoff distance, which is equivalent to a potential that is a negative constant for distances greater than the cutoff distance. These two corresponding LJ potential energy profiles are radically different (Supplemental Figure A2), with the MC barostat energy (potential U2 in Supplemental Figure A2) containing an effective step change in the potential favoring smaller pairwise distances. This inconsistency between the assumed potentials in the MC and the MD steps leads to a discrepancy between the target equilibrium lipid densities in the bilayer, with a higher target density in the MC steps compared to the dynamics, introducing an effective compressive bias in the XY plane (see Supplementary Information Section 3).

We believe the problematic systems then evolve as follows. The flattened, effective potential employed during dynamics leads to lower in-plane lipid density by promoting out-of-plane lipid fluctuations resulting in membrane thickening. Meanwhile, the MC barostat favors higher in-plane lipid densities than the dynamics biasing volume trial moves toward compression of the xy-area over expansion. This area reduction exacerbates the crowding experienced during dynamics and the bilayer further thickens. This positive feedback cycle continues, eventually buckling the membrane. By using potential or force switching, even over very short distances, the target densities are consistent with one another, and the effective compression is removed so the membranes do not buckle (Supplementary Table A1, see simulation #9 vs. #25–27). Importantly, this process does not occur when a hard cutoff is employed with either the Berendsen or the Parrinello-Rahman barostats because they calculate the pressure from the virial, which uses MD forces—not energies—to drive changes in the box size based on the difference from the target pressure.

Next, we employed an elastic energy model of the membrane that includes an energetic cost for in-plane compression together with a Helfrich-like bending energy (Helfrich) to attempt to understand why small membranes only compress while large membranes buckle (see Supplementary Information Section 1 and

Helfrich). According to this model, buckling occurs when the x/y cell dimensions decrease to the point where bending is more energetically favorable than in-plane compression, giving a quantitative relationship for when that threshold is reached (Supplementary Information Equation (9)). When combined with the estimate of compressive strain induced by employing the MC barostat with a hard cutoff (Supplementary Information Equation (19)), we arrive at an expression that predicts the critical membrane length ($L_{critical}$) beyond which initially planar membrane patches of length (L_0) buckle:

$$L_0 > L_{critical} = \sqrt{\frac{\pi\kappa R^4}{4\rho_0^2\varepsilon\lambda^6}} \propto R^2 \quad (2.1)$$

where κ is the bilayer bending modulus, ρ_0 is the initial lipid density (the inverse of the APL), ε and λ are the well depth and radius, respectively, of the LJ potential, and *R* is the applied LJ cutoff distance. Putting this together, the compressive bias stresses the membrane, and that stress tends to grow with repetitive applications of the Metropolis algorithm until either the induced strain balances the effective compressive load or the membrane buckles. Compressive elastic balance is achieved quickly with the small (L_0 = 90 Å) membrane patch by a simple elastic compression. Equation (2.1) yields an $L_{critical}$ value of 190 Å for a 10 Å hard LJ cutoff and the parameters of our simulations, correctly predicting that the small patch would not buckle while the 200 Å patch would. We conducted additional simulations to test these ideas (see Supplementary Information) including simulations with an 8 Å hard cutoff ($L_{critical}$ = 122 Å) and a 12 Å hard cutoff ($L_{critical}$ = 274 Å), and the results are all consistent with Equation (2.1). For example, a 200 × 200 Å patch with a 12 Å cutoff does not buckle, although it does show in-plane compression (#21 in Supplementary Table A1).

In conclusion, the extreme membrane distortions discussed here for the larger membrane patches only occur when using the MC barostat in combination with a 10 Å or less LJ cutoff; simply using a switching function avoids this undesirable result. While smaller patches do not undergo extreme distortion, they do deviate from experimentally derived parameters due to the effective compression; for instance, the APL shrinks from 68.7 ± 0.9 Å^2 to 65.7 ± 0.9 Å^2 when changing from a switching function to a hard cutoff (see

#17 and #15 in Supplementary Information Table A1), with the former being in general agreement with the experimental value of 68.3 ± 1.5 Å^2, (Kučerka et al.) but not the latter. These results raise a cautionary note regarding any membrane-containing simulation employing the MC barostat coupled with a hard LJ cutoff, and additional analysis would be needed to determine how other properties are impacted such as lipid-protein interactions or properties of mixed bilayers.

Methods

Initial atomic coordinates were generated using the CHARMM-GUI bilayer builder module. (Lee, Cheng, et al.) The "large" system contained 1200 POPC lipids, 53,866 water molecules with 0.15 M KCl, and had initial dimensions of 202 × 202 × 85 Å^3. The "small" system contained 240 POPC lipids, 10,766 water molecules with 0.15 M KCl and had initial dimensions of 90 × 90 × 85 Å^3. These structures were used to prepare all simulations. Two parameter sets were used in this study: (1) the Amber Lipid17 (Dickson et al.) force field with TIP3P water (Jorgensen et al.) and Joung-Cheatham ions (Joung and Cheatham) (collectively referred to as "Lipid17" or "L17" throughout), or (2) the CHARMM36 lipid force field (Klauda et al.) with CHARMM TIP3P water (Jorgensen et al.) and standard CHARMM ions (collectively referred to as "CHARMM36" or "C36" throughout).

From the starting coordinates, we initiated five separate equilibration runs: (a) "large" system with the Lipid17 forcefield in the Amber engine (*AMBER 2019*); (b) "large" system with the CHARMM36 forcefield in the Amber engine; (c) "large" system with the CHARMM36 forcefield in the OpenMM engine (Eastman et al.); (d) "large" system with the CHARMM36 forcefield in the Gromacs engine (Abraham et al.); and (e) "small" system with the Lipid17 forcefield in the Amber engine. Heavy atoms were restrained with a force constant of 1.0 kcal/mol/Å^2, and restraints were eased stepwise over 125 ps, followed by 20 ns of unrestrained dynamics. During equilibration, treatment of Van der Waals forces was done according to what is considered standard for the force field, that is, for CHARMM36 Lennard-Jones (LJ) forces were switched smoothly to zero in the range 10–12 Å, while for Lipid17 a plain cutoff of 10 Å was used. For equilibration of all simulations, a Berendsen barostat was used. All equilibration and

production simulations used semi-isotropic pressure coupling requiring the x and y dimensions of the simulation cell to scale together while z scaled freely, a target pressure of 1 atm, a 2 fs timestep, and in all cases, long range electrostatic interactions were treated using the Particle Mesh Ewald method (Darden et al.). Water molecules were kept rigid using the SETTLE algorithm, (Miyamoto and Kollman) and bonds to hydrogen atoms were converted to rigid constraints using either the SHAKE (Ryckaert et al.) (Amber and OpenMM) or LINCS (Hess et al.) (Gromacs) algorithms. All simulations in Amber and OpenMM used a Langevin thermostat with a friction coefficient of 1 ps^{-1}, while those in Gromacs used a Berendsen thermostat during equilibration and thereafter a Nose-Hoover thermostat. In all cases temperature was maintained at 310 K. Simulations using a MC barostat applied trial moves to the box vectors once per every 100 dynamics steps.

Each of the five equilibrated systems (coordinates, velocities, and box vectors) was used as the common starting point for several production trajectories with different settings and parameters outlined in Supplementary Table A1 and here in the main text.

3. HARMONIZING EXPERIMENTAL DATA WITH MODELING TO PREDICT MEMBRANE PROTEIN INSERTION IN YEAST

Membrane proteins must adopt their proper topologies within biological membranes, but achieving the correct topology is compromised by the presence of marginally hydrophobic transmembrane helices (TMHs). In this study, we report on a new model membrane protein in yeast that harbors two TMHs fused to an unstable nucleotide-binding domain. Because the second helix (TMH2) in this reporter has an unfavorable predicted free energy of insertion, we employed established methods to generate variants that alter TMH2 insertion free energy. We first found that altering TMH2 did not significantly affect the extent of protein degradation by the cellular quality control machinery. Next, we correlated predicted insertion free energies from a knowledge-based energy scale with the measured apparent free energies of TMH2 insertion. Although the predicted and apparent insertion energies showed a similar trend, the predicted free-energy changes spanned an unanticipated narrow range. By instead using a physics-based model, we obtained a broader range of free energies that agreed considerably better with the magnitude of the experimentally derived values. Nevertheless, some variants still inserted better in yeast than predicted from energy-based scales. Therefore, molecular dynamics simulations were performed and indicated that the corresponding mutations induced conformational changes within TMH2, which altered the number of stabilizing hydrogen bonds. Together, our results offer insight into the ability of the cellular quality control machinery to recognize conformationally distinct misfolded topomers, provide a model to assess TMH insertion in vivo, and indicate that TMH insertion energy scales may be limited depending on the specific protein and the mutation present.

Introduction

Protein homeostasis relies on high fidelity synthesis and sorting of folded proteins to their functional sites. Proteins entering the secretory pathway in eukaryotes are translocated through the Sec61 translocon complex into the endoplasmic reticulum (ER) (Cymer et al.). However, several barriers impede protein folding, including genetic mutations, transcription or translational errors, defects in post-translational modifications, and failure to oligomerize, each of which is impacted further by cellular stress. Fortunately, these aberrant species are recognized by ER-associated molecular chaperones. They are then retrotranslocated from the ER, polyubiquitinated, and degraded by the 26S proteasome in the cytoplasm. This process is known as ER-associated degradation (ERAD) (Vembar and Brodsky; Hampton and Sommer; Olzmann et al.; Christianson and Ye; Brambilla Pisoni and Molinari; Berner et al.).

The ERAD pathway also regulates the levels of select native proteins in response to metabolic cues (Guerriero and Brodsky).

The translocation and folding of multipass membrane proteins is particularly problematic. When the translocon encounters a hydrophobic stretch of ~19–30 amino acids (Baeza-Delgado et al.), these segments exit via a lateral gate and partition into the ER membrane (Rapoport et al.). Using various models, the characteristics that drive transfer of a transmembrane helix (TMH) from translocon homologs into a lipid bilayer have been elucidated. Critical features include the positions of polar and charged residues in and adjacent to the TMH, TMH length, and overall hydrophobicity (Spiess et al.; Junne et al.; White and Wimley; Wimley and White; Liu et al.; Hessa, Kim, et al.; Hessa, Meindl-Beinker, et al.). For example, Ile, Leu, Val, Ala, Phe, and Met are favored in TMHs because of their lipophilicity, but polar and charged amino acids are increasingly disfavored as they near the center of a TMH (Hessa, Meindl-Beinker, et al.; Zhu et al.). Curiously, a significant fraction of TMHs in multipass membrane proteins should fail to enter the bilayer based on predicted calculations of insertion free energy (Hessa, Meindl-Beinker, et al.; Öjemalm et al.), but this hurdle is overcome by information transmitted from adjacent helices (Hessa, Meindl-Beinker, et al.; Öjemalm et al.; Hedin et al.; Buck et al.; Meindl-Beinker et al.; L.

Zhang et al.; Lerch-Bader et al.). Nevertheless, little is known about how TMH hydrophobicity affects the fate of a misfolded substrate.

Herein, we explored the impact of marginal TMH hydrophobicity on ERAD by using a model dual-pass protein fused to an unstable nucleotide-binding domain (NBD) that resides in a yeast ATP-binding cassette (ABC) transporter. TMH2 of the model protein has an unfavorable free energy for insertion, resulting in deposition of the NBD into the ER lumen. We first tested the hypothesis that altering TMH2 free energy will impact degradation of the model protein. Surprisingly, the topological arrangement of the model protein did not alter the degradation profile. Our model protein also presented μs with the opportunity to examine TMH insertion in yeast. Using a series of TMH2 variants, we then discovered that particular variants have stronger than predicted effects on apparent insertion free energy. By combining physics-based energy calculations and molecular dynamics (MD) simulations, we attributed heightened membrane stability of these variants with altered helix conformation and increased hydrogen bonding.

Materials and Methods

Yeast strains, plasmids, and plasmid construction

Yeast was maintained as described previously (Adams et al.). Table S1 lists the *Saccharomyces cerevisiae* strains used in this study, and Table S2 lists the plasmids and primers. Chimera N∗ construction was described in detail elsewhere (Guerriero, Reutter, et al.). To create Chimera N∗ variants, 40 bp primers were designed to include the desired codon change in TMH2 in the center of the primer. Mutagenesis was carried out by PCR overlap extension using the pCG28 template for pCG125, pCG126, pCG127, pCG130, pCG147, pCG148, and pCG149. For some double mutants, single mutants were used as a template; for pCG128, pCG126 served as a template; for pCG129, pCG127 served as a template; and for pCG131, pCG130 served as a template. Two fragments were then generated, a 5′ fragment (Fragment A) and 3′ fragment (Fragment B), each containing the mutation encoded in their respective primers. Fragments A and B were then used in a second PCR. The two fragments were added alone for five cycles to anneal, followed by the addition of primers at the extreme 5′ (pCG119) and 3′ (pCG128) ends of the

annealed fragments to stich the fragments in another PCR cycle. The full length fragments were then digested and ligated into an empty 2μ vector downstream of the PGK promoter (empty version of pCG63) using the EcoRI and SacI restriction sites. The fragment A and B primer pairs are (5′ Fragment A/3′ Fragment A);(5′ Fragment B/3′ Fragment B), pCG131 (oCG119/168);(oCG169/128), pCG130 (oCG119/152);(oCG153/128), pCG129 (oCG119/166);(oCG167/128), pCG128 (oCG119/164);(oCG165/128), pCG127 (oCG119,150);(oCG151/128), pCG126 (oCG119/160);(oCG161/128), pCG125 (oCG119/162);(oCG163/128), pCG147 (oCG119/215);(oCG214/128), pCG148 (oCG119/213);(oCG212/128), and pCG149 (oCG119/217);(oCG216/128). The complete DNA sequence of all Chimera N∗ variants was confirmed using primers oKN54, oCG06, and oCG07.

Antibodies, immunoblot analysis, and indirect immunofluorescence microscopy

For immunoblot analysis, rat monoclonal anti-HA-horseradish peroxidase (HRP; 3F10; Roche, Basel, Switzerland) was used at 1:5000 to detect Chimera N∗. As a loading control, rabbit anti-glucose-6-phosphate dehydrogenase (A9521; Sigma-Aldrich, St. Louis, MO) was used at 1:5000. For sucrose gradients, rabbit anti-Pma1p (Abcam, Cambridge, UK) was used at 1:2500, rabbit anti-Anp1p (a gift from Sean Munro, Cambridge University, Cambridge, United Kingdom) was used at 1:4000, and rabbit anti-Sec61p was used at 1:1000 ((Stirling et al.). To detect myc-tagged ubiquitin, rabbit anti-myc (SC987; Santa Cruz Biotechnology, Dallas, TX) was used at 1:2500. After transfer to nitrocellulose, antibodies were incubated with blots overnight at 4°C, and bound primary antibodies were adorned with anti-rabbit immunoglobulin G HRP-conjugated secondary antibodies at 1:5000 for 2 h at room temperature. Bound antibodies were visualized using the SuperSignal Chemiluminescence kit (Thermo Fisher Scientific, Waltham, MA), images were captured using a Bio-Rad ChemiDoc XRS+ (Hercules, CA), and data were analyzed using ImageJ software, version 1.49b (National Institutes of Health). For indirect immunofluorescence microscopy, Chimera N∗ was detected with mouse anti-HA (12CA5; Roche) used at 1:500 and decorated with Alexa Fluor 488 goat anti-mouse at 1:500, rabbit anti-Kar2p (Brodsky and

Schekman) was used at 1:250 and detected with Alexa Fluor goat anti-rabbit at 1:500, and prolong antifade Gold with 4′,6-diamidino-2-phenylindole (Thermo Fisher) was used as a mounting agent and to detect nuclei. Indirect immunofluorescence was performed as described previously (Amberg et al.) and as reported recently (Guerriero, Reutter, et al.) using an Olympus FV1000 (Olympus, Tokyo, Japan), ×100 UPlanSApo oil immersion objective, numerical aperture 1.40.

Cycloheximide chase assays

Protein turnover was measured using a cycloheximide (CHX) chase assay in yeast expressing Chimera N∗. Cells were grown to OD600 = 0.5–1.5 in synthetic complete medium lacking uracil (−Ura) and containing 2% glucose. A 1 mL aliquot of cells was removed at the 0 min time point, and then CHX was added to a final concentration of 175 μg/mL. The culture was incubated in a shaking water bath at 26 or 37°C, as indicated, at 200 rpm. A 1 mL aliquot was removed at each time point into ice-cold tubes containing 0.5 M NaN3 (final concentration 17.5 mM), and the cells were pelleted and flash frozen. Proteins were extracted by alkaline lysis and trichloroacetic acid (TCA) precipitation (Nakatsukasa et al.). The protein pellet was disrupted with a mechanical pestle in TCA sample buffer (80 mM Tris (pH 8), 8 mM EDTA, 3.5% SDS, 15% glycerol, 0.08% Tris base, 0.01% bromophenol blue) supplemented with fresh β-mercaptoethanol (final concentration 5%), and the samples were heated to 37°C for 30 min. An aliquot of each sample was subjected to sodium dodecyl sulfate–polyacrylamide gel electrophoresis (SDS-PAGE) on a 10 or 12.5% polyacrylamide gel. Proteins were transferred onto nitrocellulose (BioTrace NT; Pall, Port Washington, NY) using a Trans-Blot Turbo Transfer System (Bio-Rad) and immunoblotted as described above.

Sucrose gradient analysis

Sucrose gradients were performed as described previously (Guerriero, Reutter, et al.). Briefly, BY4742 cells expressing HA-tagged Chimera N∗ were grown to log phase, and ~40 OD600 equivalents of cells were pelleted in a clinical centrifuge and resuspended in 400 μL of 10 mM Tris (pH 7.6), 10 mM EDTA,

10% sucrose supplemented with 2 mM phenylmethlsulfonyl fluoride, 3 μg/mL leupeptin, 1.5 μg/mL pepstatin A, and 1 mM dithiothreitol. Cells were frozen dropwise into liquid N2 and stored at −80°C. The frozen cells were then subjected to liquid N2 lysis by grinding in a prechilled mortar and pestle for ∼5 min, refreshing the liquid N2 once each minute. After thawing the yeast powder, unbroken cells were removed by centrifugation for 2 min at 2000 rpm in a microcentrifuge at 4°C. The cleared lysate was then layered on an 11 mL 20–70% stepwise sucrose gradient, and 0.5% of the lysate was retained as the load fraction. Next, the gradients were centrifuged at 100,000 × g in a Beckman SW41 rotor for 18 h at 4°C. Fractions were collected from top to bottom, and any pelleted proteins at the bottom of the tube were solubilized in TCA sample buffer. An aliquot of each fraction was mixed with TCA sample buffer and analyzed by SDS-PAGE and immunoblot analysis as described above.

Measurements of substrate ubiquitination

pdr5Δ yeast cells were transformed with a Chimera N∗ expression plasmid (construct 10) or an empty vector and pKN31 for expression of a Cu2+-inducible myc-tagged ubiquitin. Cells were grown to log phase at 26°C and treated with either dimethylsulfoxide or 20 μM MG132 for 1 h concomitant with the addition of 100 μM copper sulfate. Cells were harvested in a clinical centrifuge and washed once with ice-cold water, and pellets were stored at −80°C. Cells were lysed as described (Guerriero, Reutter, et al.), and Chimera N∗ was immunoprecipitated using anti-HA-conjugated agarose beads (Roche). Chimera N∗ was liberated from the beads with TCA sample buffer supplemented with β-mercaptoethanol and analyzed by SDS-PAGE and immunoblotting. Before antibody exposure, the nitrocellulose membrane was incubated in boiling water for 1 h to further denature polyubiquitin epitopes.

Continuum energy calculations

An idealized α-helix for the wild-type TMH2 variant in Table 2 was constructed in Avogadro 1.2.0 (Hanwell et al.), followed by minimization with ProteinPrep Wizard in Schrodinger Maestro (*Small-Molecule Drug Discovery Suite 2016–1*). From this structure, we used Pymol to create the mutants,

holding all other atoms fixed during the procedure. The high probability rotamer was always selected. Next, PARSE atomic partial charges were set using PDB2PQR (Dolinsky et al.), and we neutralized the charges on the N- and C-termini by hand. Briefly, our physics-based membrane insertion energy (ΔG) is given by:

$$\Delta G = \Delta G_{elec} + \Delta G_{np}, \quad (3.1)$$

where the electrostatic energy (ΔG_{elec}) was calculated by solving the linear Poisson-Boltzmann equation and the nonpolar energy (ΔG_{np}) was assumed to be proportional to the protein's solvent-exposed surface area with a surface tension of a = 0.023 kcal/mol/Å^2 (Table 1). The reference state for both energy contributions is the protein free in solution, and the final state is the membrane-embedded structure. ABPSmem was used to compute both energies using calls to APBS for the electrostatics (Baker et al.) and MSMS for the protein surface area calculations (Sanner et al.), with a salt concentration of 100 mM. The contribution to the nonpolar energy was linearly scaled from 0 to a for portions of the protein spanning the headgroup region. See (Marcoline et al.) for more details.

Table 3.1 Parameters for Physics-Based Model

Parameter	**Value**
Force field	PARSE
Counterions	±1|e|, 0.1 M, 2.0 Å
Temperature	298.15 K
Grid dimensions	161 × 161 × 161
Coarse grid size	300 × 300 × 300 Å3
Fine grid size	50 × 50 × 50 Å3
Protein dielectric	2
Membrane dielectric	2
Headgroup dielectric	80
Solvent dielectric	80

Parameter	Value
Hydrophobic thickness	26 Å
Headgroup thickness	8 Å
Grid center	origin
Solution method	npbe
Boundary condition	zero
Charge model	spl2
Surface model	mol
Spline width	0.3 Å
Solvent probe radius	1.4 Å
Surface sphere density	10 Å−2
Nonpolar surface tension	23 cal/mol/Å2

Table 3.2 Free Energies and Percentage of TMH2 Insertion for Chimera N∗ variants.
The ΔG_{pred} values were determined using ΔG Predictor (http://dgpred.cbr.su.se), and the ΔG_{app} values were calculated by the equation $\Delta G_{app} = -RT*\ln K_{app}$, where $K_{app} = (f_{inserted}/f_{uninserted})$ and T = 293 K. The sequence for each TMH2 variant is listed, with alterations from the native sequence (construct 10, ΔG_{pred} = 1.07 kcal/mol) indicated in bold font and underlined. The percent insertion for each TMH2 variant was determined from n = 2–4 independent experiments performed with technical replicates.

Construct #	ΔGpred (kcal/mol)	ΔGapp (kcal/mol)	TMH2 Sequence	% Insertion
1	−2.37	−1.23	RSMAVMAL**L**AA**L**V**L**VMWLSLTSW	87.6
2	−1.60	−1.75	RSMAVMALGAALVLVMWLSLTSW	90.8
3	−1.12	−1.73	RSMAVMALLAASVLVMWLSLTSW	91.4
4	−0.53	−1.91	RSMAVMALLAALVPVMWLSLTSW	92.1
5	−0.17	−1.29	RSMAVMALGAASVLVMWLSLTSW	88.9
6	0.15	−0.42	RSMAVMALGAALVPVMWLSLTSW	66.1
7	0.4	−1.01	RSMAVMALLAASVPVMWLSLTSW	81
8	0.42	−0.20	RSMAVMALGAAMVPVMWLSLTSW	58.4
9	0.57	0.47	RSMAVMALGAAAVPVMWLSLTSW	30.8
10	1.06	1.07	RSMAVMALGAASVPVMWLSLTSW	16.5
11	1.76	0.93	RSMAVMALGAA**N**VPVMWLSLTSW	16.9

The optimal membrane configuration of each construct was identified by computing ΔG for a wide range of orientations and then selecting the minimal value. Initially, the center of mass of each helix was

positioned at the origin, with the long axis of the helix aligned to the membrane normal (z axis). The helix was rotated about its long axis by an angle ψ ranging from 0 to 360° in 10° increments, and for each value of ψ, it was then tilted off the z axis ϕ about the point $\vec{P}$ = (0, 0, 21 Å) at the N-terminus. ϕ ranged from 0 to 90° in 10° increments. The energy was computed using the linearized Poisson-Boltzmann equation, with one level of focusing to a resolution of 0.51 Å/grid for each orientation producing heat maps like those shown in Figure 3.4. From each insertion energy map, we identified the lowest energy configuration and redid the calculation using the nonlinear equation with a finer, final resolution of 0.31 Å/grid. These calculations do not properly capture the energy of the uninserted state at the membrane interface, which is undoubtedly much lower energy than having the hydrophobic segments free in solution. Therefore, we shifted all ΔG values by +26.9 kcal/mol before plotting in Figure 3.5A.

The theoretical percent insertion based on Boltzmann statistics for a two-state system with experimental energy values ΔG_{app} (black curve, Figure 3.5 A) is given by:

$$P(\Delta G_{app}) = \frac{1}{1.3+e^{\frac{\Delta G_{app}}{k_B T}}} + 0.15 \qquad (3.2)$$

where under strongly destabilizing energy changes, 15% of the inserted band is still observed, whereas under strongly stabilizing conditions, 8% of the protein still fails to insert.

Molecular dynamics simulations

All-atom MD simulations of the wild-type, G10L, S13L, and P15L helices were initiated using the same TMH2 models generated for the continuum calculations. Each helix was embedded in a phosphatidylcholine lipid bilayer containing 50 lipids per leaflet and solvated in 150 mM KCl using CHARMM-GUI (Jo et al.), resulting in an average box size of 28000 atoms. These were then equilibrated in GROMACS 2018.3 (Abraham et al.) using the default equilibration scheme provided by CHARMM-GUI (Lee, Cheng, et al.) for a total of 1.0 ns each. Production simulations were run for 500 ns each using

the CHARMM36 force field (Huang and MacKerell) with a semi-isotropic pressure tensor and the Parrinello-Rahman barostat using a 5 ps^{-1} piston frequency. Temperature coupling using a Nose-Hoover extended ensemble was used with a reference temperature of 303.15 K and piston frequency of 1 ps−1. The SHAKE algorithm was used with a 2 fs time step. A nonbonded cutoff of 12 Å was used, and electrostatics were calculated using the particle mesh Ewald method, with snapshots saved every 500 ps. The distinct kinking behavior present in several simulations was initially identified by visual inspection. We then used the VMD Bendix plugin (version 1.1) to quantify these values by calculating the average local kink angle θ (defined in Figure 3.5 E, top) along the length of the helix over the entire simulation (Dahl et al.). Using a side length of 3.6, Bendix moves down the helix and calculates θ for every 3.6 residues and assigns this value to the top residue of the group while assigning linearly increasing values to the first three peripheral axis residues and linearly decreasing values to the last three, whose kink angles cannot be calculated. To quantify the helix tilt angle relative to the membrane, we computed the angle ϕ (defined in Figure 3.5 E, middle) between the helix and the membrane normal using:

$$\phi = \cos^{-1}\left(\frac{\vec{R}\cdot\hat{z}}{|\vec{R}|}\right) \tag{3.3}$$

where $\vec{R}$ is the vector from the COM of residue 2 to the COM of residue 24 and $\hat{z}$ is the membrane normal vector. Mean ϕ values in Figure 3.4 are averaged over the last 250 ns of each simulation. Finally, the total number of hydrogen bonds for residues 2–24 was calculated over the last 250 ns using the MDAnalysis with default parameters (Michaud-Agrawal et al.).

Results

To study the effect of marginal hydrophobicity on ERAD, we generated a dual-pass protein with an appended C-terminal misfolded domain (“degron”), which is sufficient to trigger proteasome-mediated degradation (Figs. 1 A and S1) (Guerriero, Reutter, et al.; Guerriero, Weiberth, et al.). The degron was modeled on an ABC transporter in *S. cerevisiae*, Sterile 6 (Ste6p) (Kuchler et al.; McGrath and

Varshavsky). Ste6p possesses two sets of 6 TMHs, each followed by a cytoplasmic NBD, which links ATP hydrolysis to the transport of the a-type mating factor (Figure 3.1 A). A 42-amino-acid truncation in the C-terminal NBD2 results in ERAD, and the substrate was termed Ste6p∗ (Loayza et al.). As a conserved member of the ABC transporter family, Ste6p is predicted to have 12 TMHs (Decottignies and Goffeau); however, most of the TMHs in Ste6p have an unfavorable ΔG for insertion (Table S3, http://dgpred.cbr.su.se) (Hessa, Meindl-Beinker, et al.; Hessa, Kim, et al.). Using a series of invertase fusions, Geller et al. validated proper insertion of the first six TMHs of Ste6p (Geller et al.). Therefore, we simplified our analysis by linking only TMH1-2 from Ste6p to the 42-amino-acid-truncated NBD2 (NBD2∗). This species was termed Chimera N∗ (Guerriero, Reutter, et al.). Although the native TMH2 in this chimeric protein segment was unable to insert into the ER membrane, the topology could be corrected by replacing TMH2 with a 20-amino-acid poly-Ala/Leu sequence (Marcoline et al.). When adopting its proper (inserted) topology with NBD2∗ in the cytoplasm, Chimera N∗ does not utilize its single available consensus site for the addition of an N-glycan moiety (NxS/T). Notably, the N-glycan consensus site is present in the ER lumenal loop between TMH1 and TMH2 in Chimera N∗; however, its proximity to the lipid bilayer prevents access to the oligosaccharyl transferase complex (Nilsson and von Heijne). In contrast, failed insertion of TMH2 deposits NBD2∗ into the ER lumen, granting access to four N-glycosylation consensus sites that are present in NBD2∗ (Figure 3.1 A). This attribute provides a quantitative method to monitor THM2 insertion into the ER.

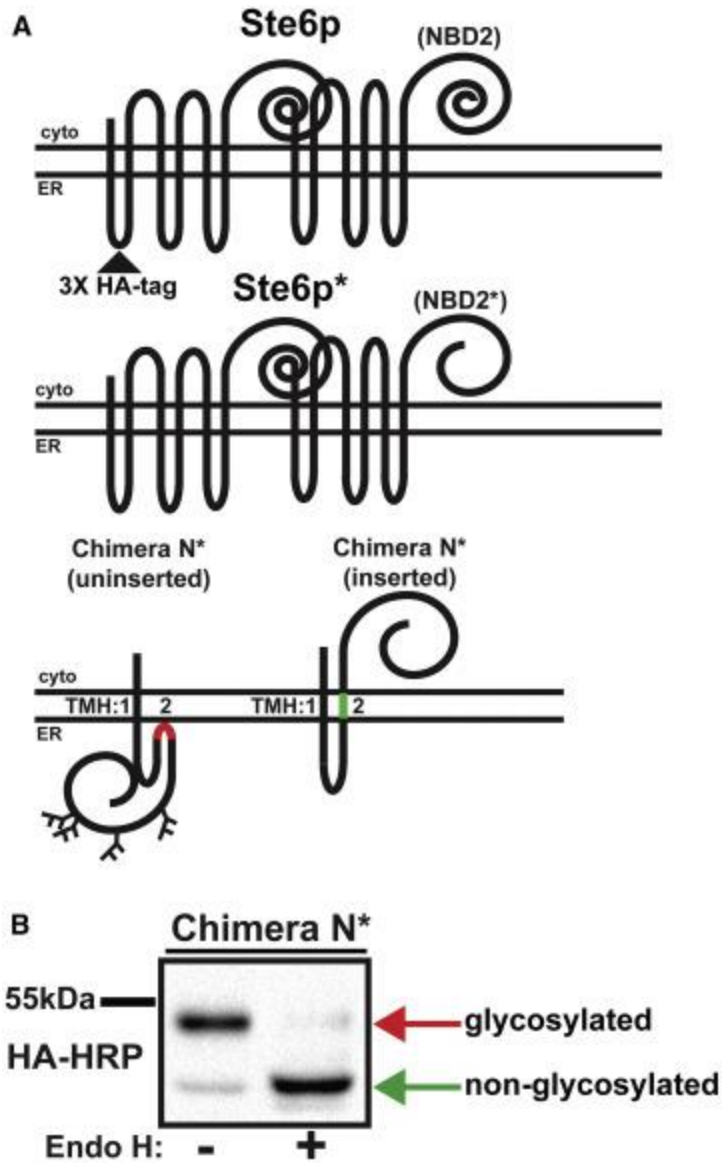

Figure 3.1 The design of a model substrate to measure transmembrane domain insertion in yeast. (A) A cartoon depicting the topology of Ste6p and Ste6p∗ and the two topologies adopted by Chimera N∗ is given. Each construct has a 3× HA-tag in the lumenal loop between TMH1 and TMH2. Chimera N∗ was made by internal deletion of amino acids 141–1042 in the coding sequence for 3× HA Ste6p∗. Chimera N∗ displays dual topologies, with TMH2 residing inside the ER lumen (left, red), which consequently deposits NBD2∗ into the ER lumen and allows for N-glycan addition. Alternatively, TMH2 can insert properly into the membrane (right, green), which prevents acquisition of N-linked glycans. (B) *S. cerevisiae* strain BY4742 expressing Chimera N∗ under the control of a low-expression ADH promoter (pCG28) was grown to log phase, and cellular protein was extracted and incubated in the absence or presence of Endo H. Chimera N∗ was detected by SDS-PAGE and subsequent immunoblotting with anti-HA antibody. Red and green arrows to the right of the immunoblot mark the positions of the glycosylated and non-glycosylated forms, respectively.

The predicted ΔG for insertion of TMH2 (ΔGpred) calculated using ΔGPredictor (http://dgpred.cbr.su.se/) is 1.06 kcal/mol (Hessa, Kim, et al.; Hessa, Meindl-Beinker, et al.). By examining the electrophoretic mobility of Chimera N∗ after expression at low copy number (pCG28, Table S1) in wild-type yeast (BY4742, Table S2), the protein largely adopted the uninserted orientation. This was evidenced by a slower than predicted migration pattern compared to the unglycosylated species (~43 kDa; Figure 3.1 B, left). We next treated cell extracts with the bacterial enzyme endoglycosidase H (Endo H), which removes N-glycan moieties. Digestion with Endo H confirmed that the slower-migrating species had acquired N-linked glycans because of aberrant localization of NBD2∗ into the ER lumen (Figure 3.1 B, right). Based on the observed shift in mobility, all four N-glycan acceptor sites in NBD2∗ were used.

As noted above, replacing TMH2 with a poly-Ala/Leu sequence corrects TMH2 topology, resulting in a dual-pass substrate (with NBD2∗ in the cytosol) that is targeted for ERAD (Guerriero, Reutter, et al.). Therefore, to test whether the single-pass substrate Chimera N∗ is also an ERAD substrate, we examined its fate. A hallmark of ERAD substrates is retention in the ER even though no peptide ER retention signals are present. This phenotype is typified by the disease-causing allele F508del in the cystic fibrosis transmembrane conductance regulator (CFTR), which is completely ER-retained (Cheng et al.). We first used indirect immunofluorescence microscopy and confirmed Chimera N∗ residence in the ER based on a perinuclear and cortical staining pattern that is typical of the ER in yeast. In addition, Chimera N∗ staining overlapped with an ER-localized chaperone, Kar2p (Figure 3.2 A). ER residence was further confirmed by sucrose gradient analysis. Because the ER is bound by ribosomes engaged in translation, the ER can be isolated from the plasma membrane by differential centrifugation because of its increased density. We observed that Chimera N∗ comigrated with Sec61p but not with a plasma-membrane-resident protein (Figure S2 A). To determine whether Chimera N∗ is an ERAD substrate, we next examined degradation via CHX chase. CHX is a bacterial toxin that binds the ribosome and halts new protein synthesis (Schneider-Poetsch et al.). Therefore, CHX treatment allows μs to monitor the turnover of a pool of Chimera N∗ over time. The CHX chase was performed in a pdr5Δ yeast strain, which lacks a

major drug pump and allows for treatment with a proteasome inhibitor, MG132 (Lee and Goldberg; Gaczynska and Osmulski). As shown in Figure 3.2 B, Chimera N∗ degradation was delayed in MG132-treated yeast, indicative of ERAD. Because Chimera N∗ was partially stabilized by treatment with MG132, we examined the potential contribution of yeast vacuolar proteases on Chimera N∗ degradation in a strain that also lacked vacuolar activity (pdr5Δpep4Δ). In some instances, a portion of a misfolded protein can be trafficked from the ER and degraded in the yeast vacuole, which is equivalent to the lysosome (Sun and Brodsky). However, we found that the overall degradation level was unchanged in pdr5Δpep4Δ yeast, suggesting no vacuolar involvement. Additionally, it has previously been observed that high-level expression of an ERAD substrate can redirect a portion of the misfolded protein to the vacuole (Spear and Ng). However, comparable results were obtained regardless of whether the substrate was expressed at high or low levels (Figure S2, B and C).

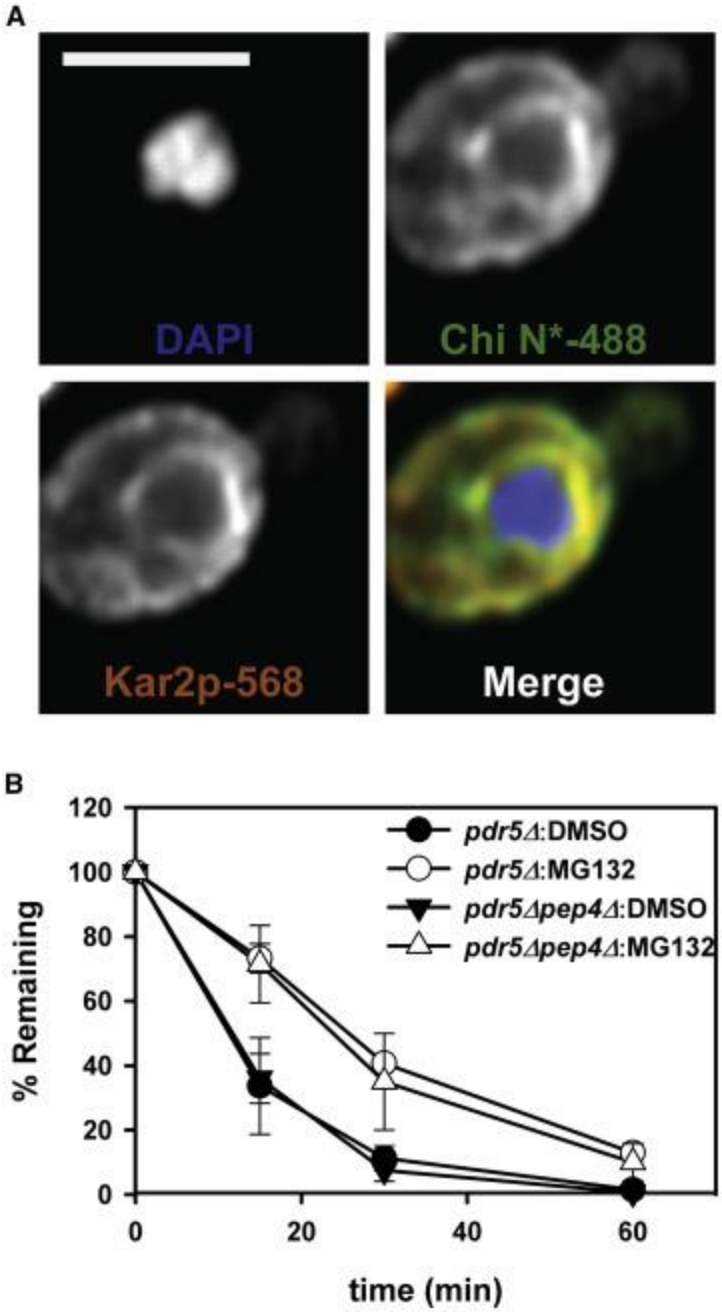

Figure 3.2 Chimera N∗ resides in the ER and is degraded by ERAD.
(A) The residence of Chimera N∗ in the cell was investigated by indirect immunofluorescence using mouse anti-HA antibody (Chimera N∗, green), rabbit anti-Kar2p (ER lumen, red), and 4′,6-diamidino-2-phenylindole (nuclei, blue). Primary antibodies were decorated with Alexa goat anti-mouse 488 and goat anti-rabbit 568. Images were captured using a confocal microscope, and a slice through the plane of the ER is shown. Scale bars, ~5μm. (B) Chimera N∗ was expressed at high copy in pdr5Δ (circles) or pdr5Δpep4Δ (triangles) yeast. Before CHX chase analysis, cells were preincubated at 26°C with either dimethylsulfoxide (filled symbols) or 100 μM MG132 (open symbols) for 20 min and chased for the indicated times. Graphed data represent the means ± SD from a representative experiment of n = 4 independent experiments for pdr5Δ and n = 1 performed with four technical replicates for pdr5Δpep4Δ.

A critical step in targeting a substrate to the proteasome is the addition of a polyubiquitin chain by E3 ubiquitin ligases (Vembar and Brodsky). Therefore, we next examined Chimera N∗ polyubiquitination and observed an increase in the polyubiquitin ladder after treatment with MG132 (Document S1. Figs. S1–S3 and Tables S1–S4, Document S2. Article plus Supporting Material). Taken together, our data demonstrate that despite its unanticipated topology, Chimera N∗ is an ERAD substrate.

To explore the contributions of diverse TMHs on ER membrane insertion and ERAD, we designed Chimera N∗ variants using ΔG Predictor to determine ΔGpred. The ΔG Predictor tool is a knowledge-based energy scale (herein referred to as a bioinformatics scale) built from in vitro studies on the insertion of artificial TMHs (Hessa, Kim, et al.; Hessa, Meindl-Beinker, et al.). To this end, we generated 10 Chimera N∗ variants with altered TMH2 sequences (Table 3.2). As noted above, the ΔGpred for TMH2 in Chimera N∗ is 1.06 kcal/mol (Table 3.2, construct 10). We then focused on altering residues near the predicted middle of TMH2 because deleterious residues in this position should have the strongest effect on insertion (Hessa, Meindl-Beinker, et al.). We next expressed the variants in yeast and quantified insertion (Figure 3.3 A; Table 3.2). Although the Chimera N∗ degron (NBD2∗) remains constant in each variant, as ΔGpred for TMH2 decreases, the location of NBD2∗ shifts from primarily the ER lumen to the cytoplasm. Therefore, we anticipated different degradation rates for the two forms of Chimera N∗ because the ER lumen and cytosol contain unique chaperones and quality control factors. Unexpectedly, we found that the degradation profiles of the inserted and uninserted forms of construct 8 (ΔGpred = 0.42 kcal/mol)—which is the most conformationally mercurial variant (58% insertion)—were indistinguishable (Figure S3 A). The same result was evident when comparing the inserted forms of construct 1 and construct 8 (Figure S3 B). However, a modestly slower degradation rate was observed when we compared the uninserted forms of construct 8 with construct 10, which contains the wild-type TMH2, or construct 11, which contains the least hydrophobic TMH2 (Figure S3 C). This kinetic effect was only observed at the extreme end of the tested hydrophobicity range and may represent altered chaperone protein recognition of the unfavorable helix deposited into the ER lumen.

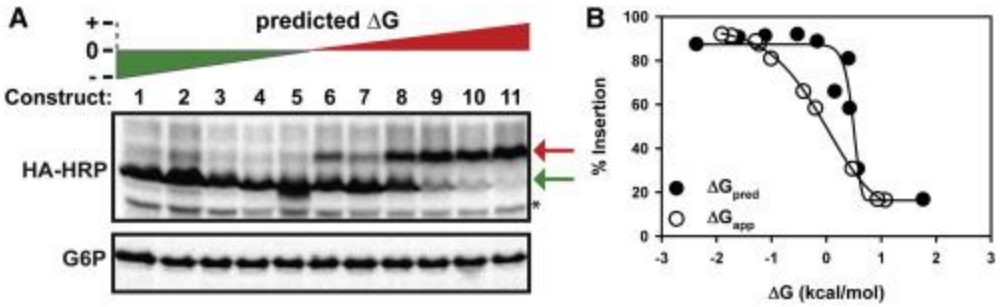

Figure 3.3 The predicted and measured insertion of Chimera N∗ in yeast.
(A) *S. cerevisiae* expressing Chimera N∗ variants was grown to log phase, cellular proteins were extracted, and the Chimera N∗ species were resolved by SDS-PAGE and immunoblotted to detect the HA tag. Variants were loaded from left (negative ΔG, green triangle) to right (positive ΔG, red triangle) in the order listed in Table 2. The red and green arrows to the right mark the positions of the noninserted and inserted forms, respectively. ∗ denotes a background band that migrates beneath the inserted form. A representative HA-HRP blot is shown, and the corresponding glucose-6-phosphate dehydrogenase blot serves as a loading control from n = 2–4 independent experiments. The percentage insertion was determined by the following equation: % inserted = $(f_{inserted}/(f_{inserted} + f_{uninserted})) \times 100$. (B) The data from part (A), displayed in Table 2, were plotted against ΔG_{pred} and ΔG_{app} and then fitted to a five-parameter sigmoidal equation using SigmaPlot.

The use of Chimera N∗ to decipher effects of TMH hydrophobicity on topology is reminiscent of a previous model based on an *Escherichia coli* leader peptidase reporter, which possesses 2 TMHs and an engineered "H-segment." The use of this substrate helped define how amino acid composition and position impact TMH insertion (Hessa, Meindl-Beinker, et al.; Meindl-Beinker et al.; Whitley et al.; Saaf et al.; Lundin et al.). Many of these studies were performed in dog pancreas microsomes. Although cell-free protein translation systems provide valuable insights, the rates of protein translation are slower in vitro than in cells, and the composition of key cytoplasmic factors that affect protein targeting to the ER, translocation, and quality control differ. Thus, it was vital to determine how ΔG_{pred} values correlate with the experimentally determined apparent free energy (ΔG_{app}) values for a substrate in its native environment, i.e., in yeast. We found that many TMH2 alterations predicted to have a minimal effect on ΔG_{pred} actually had a large impact on the ΔG_{app}, resulting in a much larger spread in ΔG_{app} values. For example, construct 10 (ΔG_{pred} = 1.06 kcal/mol) and construct 7 (ΔG_{pred} = 0.40 kcal/mol) insertion efficiencies were ∼17% and 81%, respectively, although they differ only by the presence of a Gly or Leu at position 10. Moreover, when the percent insertion versus ΔG_{pred} and ΔG_{app} was examined using a

nonlinear regression, the point at which 50% of TMH2 is inserted (I50) corresponded to a ΔG_{pred} of 0.49 kcal/mol instead of the anticipated 0 kcal/mol, based on Boltzmann statistics used to compute the experimentally derived apparent free energy (Figure 3.3 B). The discordance between the predicted and apparent ΔG values might reflect the significance of performing this study in vivo and highlights the importance of analyzing insertion parameters of TMHs in native environments.

To gain a better understanding of the insertion free energies of the TMH2 variants, we explored membrane stability with a physics-based model. In the absence of any structural information, we created idealized α-helices corresponding to each sequence in Table 2 and then computed their stabilities in the membrane compared to solution using a model that captures protein electrostatics and nonpolar stabilization in the membrane (Guerriero, Reutter, et al.; Marcoline et al.). We performed a scan over all angular orientations and identified the optimal inserted state (Figure 3.4). These calculated energy values (Table S4) were all shifted by a constant offset to account for the uninserted state at the membrane interface and then plotted (green dots) along with ΔG_{pred} (black circles from Figure 3.3 B) in Figure 3.5 A (bottom). The physics-based calculations span nearly 10 kcal/mol in predicted stabilization energies, whereas ΔG_{pred} spans only 4 kcal/mol. Importantly, the former calculations more closely match the range of expected insertion probability values based on a two-state Boltzmann distribution (black curve), whereas the bioinformatics values jump from poorly inserted to highly inserted over a very narrow energy range. This discrepancy between scales is not surprising because bioinformatics scales often produce single amino acid insertion energies that are much smaller than physics-based values (MacCallum et al.).

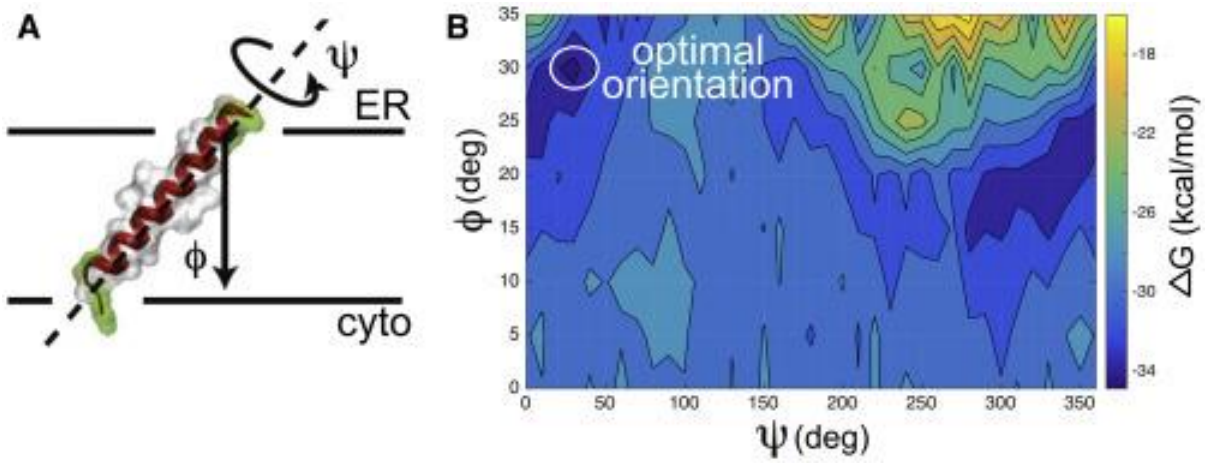

Figure 3.4 Calculation of optimal insertion orientation.
(A) Definition of angles describing helix orientation in the membrane is given. (B) Insertion energy of the physics-based continuum model based on Equation 1 of the supplement for the wild-type helix is shown as a function of helix rotation (ψ) and tilt angle (ϕ). The minimal energy value (circle) used to compute energies in Figure 5 A is highlighted. The energy barrier corresponding to embedding the end of the helix in the membrane can be seen from the high energy values from ϕ = 45–70° (yellow).

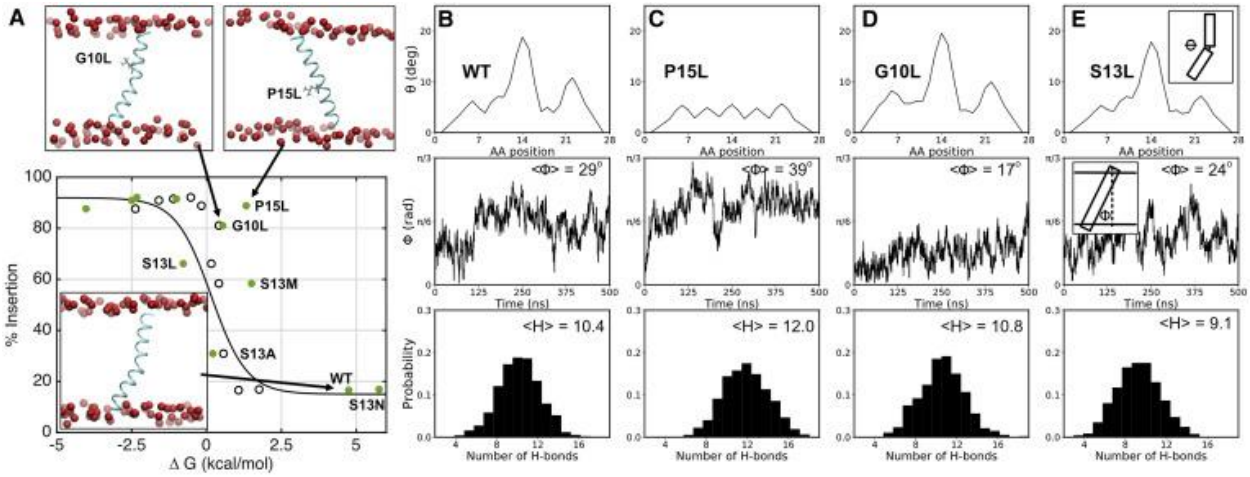

Figure 3.5 Physical models of insertion stability and molecular simulations.
(A) Energy values were derived from our physics-based energy model computed for each TMH2 variant and plotted against the measured percent insertion (green dots). ΔG_{pred} data are from Figure 3 B (black circles). Percent insertion predicted for a two-state Boltzmann distribution with energy difference ΔG bounded between 15 and 92% is shown (black curve). Insets show representative MD snapshots of the wild-type (WT) and P15L and G10L variants with mutated residues shown as licorice, protein backbone in a new cartoon, and headgroup phosphate atoms as red spheres. (B–E) Simulation details for the wild-type (B), P15L (C), G10L (D), and S13L (E) simulations are shown. Top: the average kink angle θ (defined in last panel) along the helix was computed, revealing large kinks at position 14 for wild-type and G10L and a straight helix for P15L. Middle: the angle ϕ that the helix makes with the membrane normal (defined in last panel) is shown. The average over the last half of each simulation is shown in the upper left corner. Bottom: a histogram of total backbone hydrogen bonds through the membrane span over the trajectory is shown. The average value computed over the last half of the simulation is shown in the upper left corner.

Nonetheless, two TMH2 variants are more stable in the membrane than predicted by either the bioinformatics or the physics-based models: G10L and P15L. To understand why these helices are so stable, we carried out all-atom MD simulations on the segments as well as the wild-type segment embedded in a phosphatidylcholine bilayer. It became immediately clear that the helices adopt different structural conformations. Most striking, the wild-type and G10L helices adopt a ~20° kink in the middle of the membrane at P15, in excellent agreement with previous simulation studies of proline-containing helices (Cordes et al.), but this kink is absent in P15L (top panels, Figure 3.5, B–E, and insets of Figure 3.5 A). Straightening the helix allows P15L to make 1.6 more backbone hydrogen bonds throughout the membrane spanning region than the wild-type TMH (bottom panels, Figure 3.5, B and C), which is more than the expected value of 1 for Pro removal. Although G10L still kinks, it also makes almost 0.5 more hydrogen bonds on average than the wild-type segment, and this increase likely arises from removing the flexible Gly. Membrane hydrogen bonds have the potential to be very strong in the low dielectric of the membrane (Cao et al.), and MD therefore supports our experimental observation that G10L and P15L stably integrate into the ER. The three segments also adopt different conformations in the membrane with G10L more aligned along the membrane normal (z axis), P15L adopting a 39° angle with respect to the z axis, and the wild-type segment exhibiting a more moderate angle (29°, middle panels, Figure 3.5, B–E). The physics-based model predicted the S13L mutation to be the most stabilizing of all single-point mutations, and the experiments revealed a greater than 40% increase in insertion probability over the wild-type. This large stabilization arises because the optimal membrane insertion places the polar serine in the middle of the membrane, and serine has a much higher insertion free energy than leucine, consistent with detailed free-energy calculations on isolated amino acid side chains (MacCallum et al.) and biology-based scales (Hessa, Meindl-Beinker, et al.; Moon and Fleming). Nonetheless, we wanted to explore why S13L was less stabilizing than G10L or P15L. Thus, we also carried out all-atom MD simulations on S13L to determine whether the removal of polar side chains in the core dramatically impacted the helix. Like the other proline-containing structures, S13L kinks at P15 (top panel, Figure 3.5 E), and the orientation is similar to the wild-type (middle panel, Figure 3.5 E). Not surprisingly, the loss

of hydrogen-bonding capabilities of the serine side chain upon mutation to leucine reduced the average hydrogen bonding of the entire helix by a little more than one hydrogen bond compared to the wild-type, two compared to G10L, and three compared to P15L (bottom panel, Figure 3.5, B–E). Therefore, we believe that the stabilization of S13L is largely due to better electrostatics and an increased nonpolar component, but the reduced hydrogen bonding offsets the stability compared to G10L and P15L. Overall, our simulations reveal that the mutations influence the conformation and membrane insertion in a manner that is not fully captured in either our physical model or in the bioinformatic scale. The physics-based model also fails to predict the stabilizing influence of S13M, and this may result from several sources, including overestimating the electrostatics of methionine in our continuum electrostatic calculations, undersampling of protein conformational changes, or details of the uninserted conformation.

Discussion

Herein, we report on a model dual-pass membrane protein that acts both as a reporter for membrane protein quality control and TMH insertion. For the most topologically frustrated Chimera N∗ variant with ~50% TMH2 insertion, we observed equivalent ERAD efficiencies between the inserted and uninserted forms (Figure S3 A). This result was surprising, given previous observations that topologically distinct isoforms of aquaporin 1 and rhodopsin are differentially engaged by the cellular proteostasis machinery (Buck and Skach; Roushar et al.). For example, TMH7 in rhodopsin is marginally hydrophobic because of a large number of polar and charged residues, and altering residues in the middle of TMH7 dramatically impacted the total and cell surface levels of rhodopsin, presumably through degradation of aberrant topomers (Roushar et al.). In contrast, Chimera N∗ is a quality control substrate regardless of whether TMH2 was inserted or uninserted. Therefore, any differences in degradation most likely stem from differential recognition of NBD2∗ by ER lumenal or cytoplasmic quality control machinery. An additional difference between our work and previous studies is that Chimera N∗ has only two TMHs as opposed to six (for aquaporin 1) or seven (for rhodopsin). The relatively low complexity of Chimera N∗

may allow the ERAD machinery to act more efficiently to remove both the uninserted and inserted forms. Another consideration is the route by which some integral membrane ERAD substrates are degraded. For Chimera N∗ (construct 10), the majority of the protein adopts a single-pass topology with a marginally hydrophobic TMH1 as the only membrane anchor (Table S3). Previously, it was demonstrated that single-pass proteins with marginal TMHs can completely pass into the ER lumen before they are retrotranslocated to the cytoplasm and degraded (Feige and Hendershot). However, this does not appear to be the case for Chimera N∗ because the protein remains membrane-associated in the presence of sodium carbonate, and degradation remains robust in the absence of a functional copy of the ER lumenal Hsp70, BiP (unpublished data). Interestingly, for the Chimera N∗ variants in which TMH2 was primarily uninserted, we observed different degradation rates (Figure S3 C). As noted above, in this case, decreased degradation as TMH2 becomes less favorably inserted may result from altered chaperone recognition. Our study also represents the first analysis, to our knowledge, of TMH insertion for a dual-pass yeast transmembrane protein in its native environment. As anticipated, there is an overall correlation between the ΔG_{pred} and ΔG_{app} values (Pearson correlation coefficient, R = 0.80). However, the absolute magnitude of the apparent free-energy changes is much larger, which is in better agreement with simulation/physics-based scales (Marcoline et al.; MacCallum et al.). Additionally, we noted discordance when comparing ΔG_{pred} and ΔG_{app} values at 50% percent insertion (Figure 3.3 B). These differences might reflect the contributions of endogenous cytoplasmic factors and/or a more rapid rate of translation in vivo, both of which could impact TMH insertion. In fact, a previous study comparing the ΔG_{app} in vitro and in BHK cells measured a difference between microsome and cell-based data of ∼−0.5 kcal/mol (Hessa, Kim, et al.). We observed a remarkably similar shift in I50 between the ΔG_{pred} and ΔG_{app}, (0.49 kcal/mol; Figure 3.3 B). Our data are also in good agreement with a previous study examining a leader peptidase reporter (described above) expressed in yeast. The addition of a single Leu to the engineered H-segment reduced ΔG_{app} by 1.8 kcal/mol (from 0.46 to −1.34 kcal/mol) (57), which is comparable to the 1.3 kcal/mol reduction (construct 10 versus 6) we observed.

Although ΔG Predictor provides a powerful tool to analyze insertion energies of TMHs, there are some limitations in its predictive power. For example, ΔG Predictor fails to identify Ste6p's TMH6 as an inserted helix because of the presence of a high number of polar and charged residues (Table S3). Thus, TMH6 insertion likely depends on interactions with neighboring helices, as shown for other ABC transporters (Enquist et al.; Carveth et al.; Tector and Hartl). We note that many of the rules that govern membrane protein insertion have been defined using model proteins with mostly favorable TMHs (Hessa, Meindl-Beinker, et al.; Meindl-Beinker et al.; Whitley et al.; Saaf et al.; Lundin et al.), but these studies do not take into account complex interactions between stably integrated TMHs and those with positive ΔG_{pred} values. For example, although Ste6p has 12 TMHs, only TMH4 ($\Delta G_{pred} = -1.20$ kcal/mol) and 10 ($\Delta G_{pred} = -1.25$ kcal/mol) have favorable free energies of insertion (Table S3). Therefore, the insertion of distinct Ste6p TMHs likely depends on intimate interactions with neighboring helices to achieve the proper topology. In addition to interhelix interactions, it was also recently shown that the 100-amino-acid-residue region C-terminal to a marginally hydrophobic TMH influenced insertion efficiency, indicating that the conformation of a nascent polypeptide as it emerges from the ribosome can influence existing TMHs (Junne and Spiess). Overall, the rules governing the insertion of TMHs into biological membranes continue to evolve.

Many disease-causing integral membrane proteins have been linked to ERAD (Guerriero and Brodsky), including aquaporin 2, polycystin 2, CFTR, and rhodopsin, all of which have mutant variants in predicted TMHs (Bichet et al.; Watnick et al.; Patrick et al.; Illing et al.). For channel proteins, such as CFTR, TMH mutations can disrupt critical pore residues necessary for ion permeation (Sheppard et al.; Hämmerle et al.), but they can also disrupt pore architecture, folding, and maturation (Patrick et al.; Cui et al.). Therefore, our data have implications for understanding the factors that influence TMH insertion in both normal and diseased states. Furthermore, our findings highlight the need for more studies utilizing a combination of computational and in vivo approaches to examine the relationship between positional effects of amino acids and adjacent TMHs on insertion.

4. A SIMPLE CONTINUUM MODEL OF THE MEMBRANE PREDICTS TENSION SENSING WITHOUT IN-PLANE AREA EXPANSION

Mechanosensitive ion channels are membrane proteins that open and close in response to physical forces in their environment. While some, like the spring-shaped NompC channel involved in soft touch, are thought to sense external force perpendicular to the membrane directed along the long-axis of the channel, many open in response to tension in the membrane. An established model for how in-plane tension energetical couples to channel opening was initially developed for the mechanosensitive channel of large conductance (MscL), and it posits that the energy of opening is equal to the area expansion of the protein times the tension, thus scaling linearly with membrane tension (Perozo, Cortes, et al.). This model has been extended to other channels like Piezo and the mechanosensitive channel of small conductance (MscS) (Mulhall et al.; Bass et al.). However, recent cryo-EM structures of MscS in lipid nanodiscs corroborated by molecular dynamics simulations revealed that channel opening involves only minor changes in area expansion and instead is characterized by large membrane deformations induced by the closed state that resolve as the channel opens (Park et al.). Here we employ careful analysis of coarse-grained molecular dynamics simulations to inform a model that uses continuum membrane mechanics to predict the energetics of these different bilayer configurations, and we recall the established result that membrane deformations alone scale super-linear in tension – a possible explanation for how the deformed closed state is destabilized under high tension. Our model lends insight into the intrinsic energetic difference of MscS in the open and closed states and the strained state of the bilayer, but most importantly it expands the paradigm for how membrane proteins sense tension.

Introduction

Ion channels respond to a wide array of environmental cues including small molecules, membrane voltage, temperature, and local forces. Channels that respond to force, such as K2P channels which produce potassium leak currents to stabilize the resting membrane potential in tissue (Natale et al.), Piezo channels which affect processes like bone and blood development and itch (Yang et al.; Hill et al.), and NompC which affects soft touch and locomotion (Jin et al.), are mechanosensitive. Mechanosensation occurs in all kingdoms of life from archaea to eukaryotes, and channels have evolved several different mechanisms to sense force. While some proteins, like NompC sense force because they are physically tethered to the cytoskeleton (Jin et al.; Wang et al.), other proteins, like MscL, sense force directly through the membrane (Perozo, Cortes, et al.).

MscL and its bacterial neighbor MscS were the first known mechanosensitive proteins, acting as safety valves to reduce osmotic pressure across the bacterial membrane when the ionic composition of the extracellular space quickly changes (Levina). Work by the Rees lab revealed the first crystal structures of these channels (Chang et al.; Bass et al.) in their closed states, though with very different architectures. More recent cryo EM structures have revised our understanding of MscS architecture by showing the transmembrane-adjacent helices to be on the opposite side of the membrane than previously thought (Reddy et al.). Because of this change in our structural understanding, MscS mechanosensation is not as well understood as that of MscL.

There are many potential models for direct mechanosensation through the bilayer, which typically rely either on contact with specific lipids or bulk membrane properties. Those which rely on specific contacts treat individual lipids like “ligands” where the interactions between the lipid-ligand and key residues drive the protein response, not unlike small molecule binding drives the conformational change of a host of ion channels such as the glycine and acetylcholine receptors. One example in this class is the “dragging model” proposed for MscL wherein a lipid moves away from the center of the protein in response to tension in the membrane and a tightly interacting TM2 helix moves outward along with it, thus driving the shutter-opening motion by which MscL gates (Cox et al.). Conversely, models which rely on bulk

membrane properties suggest that proteins respond to changes in curvature (Perozo, Kloda, et al.) or hydrophobic mismatch (Harroun et al.). In particular, (Wiggins and Phillips) used the experimentally observed tension dependence of MscL channel opening (Sukharev et al.; Perozo, Cortes, et al.; Perozo, Kloda, et al.) to analytically describe MscL gating as a two-state system dependent on protein conformation and membrane deformation, which is driven by the balance between applied membrane tension and hydrophobic mismatch, not reliant on specific ligand binding sites.

Recent structural and simulation-based work from Park and company has put forward a new model of MscS mechanosensation that also relies on bulk membrane properties but is quite different from any previous model discussed (Park et al.). This "membrane deformation" model posits that MscS senses tension in the membrane by exposing deep hydrophobic pockets within each of the 7 subunits that are occupied by multiple lipids in the closed state effectively pulling the lower leaflet of the membrane "down" toward the cytoplasm, thus creating a massive membrane deformation. Meanwhile, the open state of the channel closes the pockets blocking lipid access resulting in a flat undeformed membrane. These deformations do not rely on specific lipid contacts as the pocket lipids are dynamic and can diffuse freely back into the bulk membrane, and importantly, it was suggested that the blocking of these hydrophobic pockets in the open state does not significantly increase the in-plane area of the protein. This last result has essentially made it unclear where membrane tension sensing arises for MscS, as it is not understood how membrane tension couples to the conduction state of the channel in the absence of an area expansion. Here we show that this membrane deformation can be qualitatively reproduced using a fast, simplified model based on continuum elasticity theory (Marcoline et al.; Argudo, Bethel, Marcoline, and Grabe) that was updated to include novel information from recent cryo EM structures and coarse-grained molecular dynamics (CGMD) simulation data generated here but originally posited by Park *et al*. These numeric elasticity calculations, supplemented with analytical solutions that incorporate ideas introduced in earlier models about super-linear scaling of membrane deformations with tension (Wiggins and Phillips), serve as a framework for probing mechanosensation. These combined physical methods allow μs to explain how tension might be sensed by MscS via membrane deformation, rather than in-plane area expansion.

Results

Careful analysis of coarse-grained simulations reveals important biophysical features. An initial quantitative description of the equilibrium membrane shape around MscS in the closed and open states was generated using 21 μs of Martini 2.2 CGMD simulation data. Membrane average surfaces were then generated according to the procedure described in the Methods, where lipid glycerol groups are interpolated onto a grid and grids are averaged over time. The average membrane shape for the closed state (Figure 4.1A, top) is striking, with seven large hydrophobic pockets that each draw in several lipids from the lower membrane leaflet, causing wave-like membrane deformations with an amplitude of ~25 Å as reported by the Faraldo-Gomez group (Park et al.). At least 2-3 lipids reside within each pocket at a time, although they are dynamic and exchange freely with the undeformed region of the bilayer away from the protein. This deformation pattern follows a $cos(7\theta)$ form in the angular direction and has a very steep contact angle (up to 75°) with the protein that also varies azimuthally. The upper leaflet is mostly flat with only a minor downward deflection at the point of contact with the protein. Conversely, the open state exhibits very little deformation of the bilayer around the protein (Figure 4.1A, bottom). In both the open and closed states, there are 14 'hook lipids' from the upper leaflet that fill small divots between TM1 helices on the outward-facing side, as previously observed (Reddy et al.; Y. Zhang et al.).

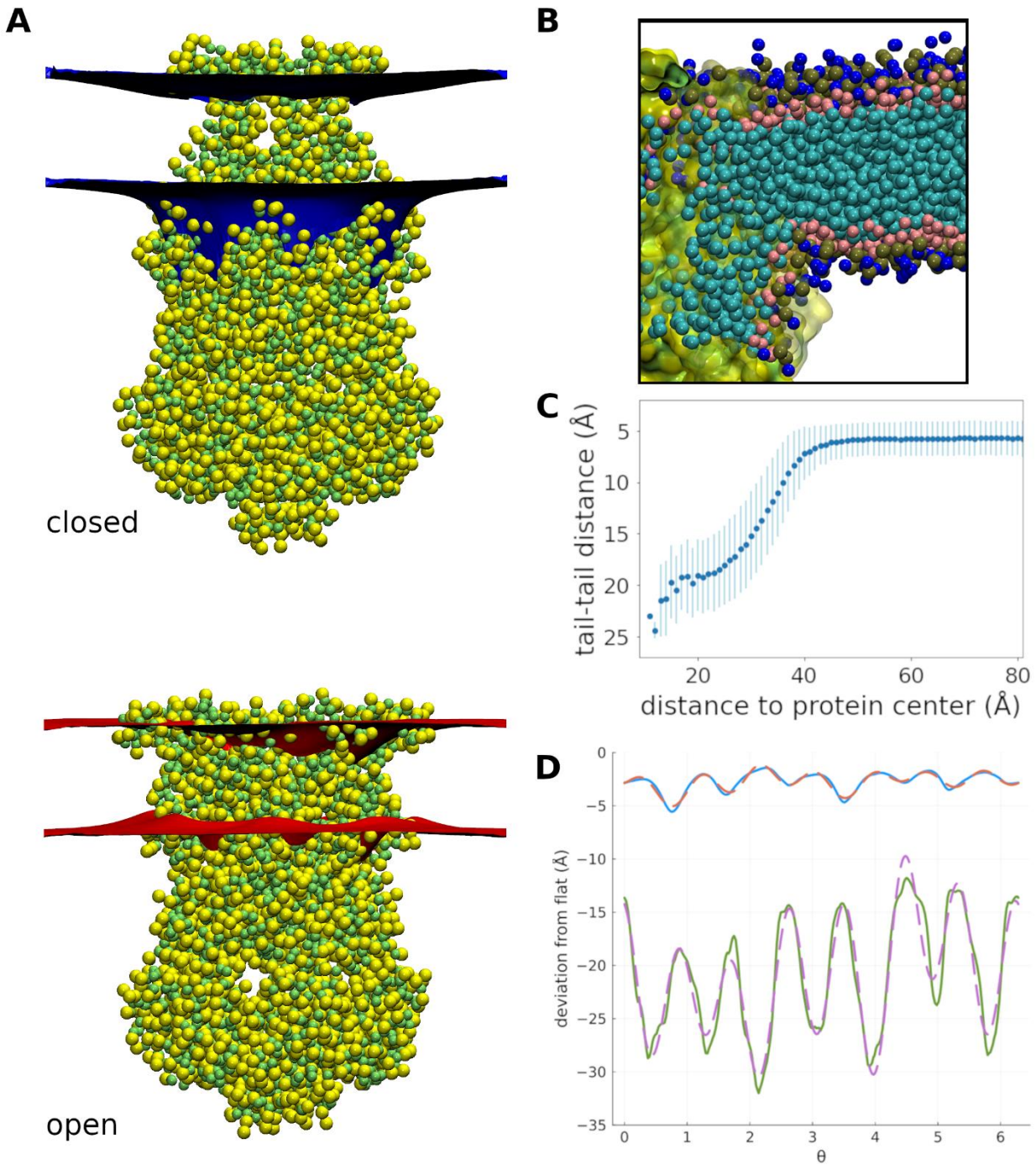

Figure 4.1 Key observations from coarse-grained simulations of MscS.
(A) Top: average membrane shape (blue) around the closed state (yellow, PDB ID 6PWP) based on 11 μs of simulation data. Bottom: average membrane shape (red) around the open state (yellow, PDB ID 8DDJ) based on 10 μs of simulation data. (B) Close-up of lipids around one of the seven hydrophobic pockets of the closed state. Lipids are shown as coarse-grain beads, with ammonium group beads in blue, phosphate groups in brown, glycerol groups in pink, and hydrocarbons in cyan. Protein is shown as transparent yellow; some protein residues are hidden for visual clarity. (C) Average minimum distance between terminal (C4A/C4B) lipid tail beads in opposing leaflets as a (Figure caption continued on the next page.)

(Figure caption continued from the previous page.) function of radial distance from the center of the closed channel (± S.E.) (D) 2-dimensional representation of the membrane boundary around the closed channel as seen in A. Upper and lower boundaries are shown as solid lines that have been shifted so the flat membrane is at zero, and the seventh order approximations are shown as dashed lines.

Simulation results inform a continuum elastic membrane model. Based on these observations from our simulations, we make the following assumptions for an updated continuum membrane model. First, deflections in the upper leaflet of the bilayer area minor compared to the lower leaflet, so we only consider deformations of the lower leaflet. Observed deviations are less than 5 Å in height, which is negligible compared to the deviations of ~30 Å observed for the lower leaflet (Figure 4.1B, D). Second, the lipid tails of the lower leaflet adjacent to the protein are disconnected from the upper leaflet tails because they are in close contact with hydrophobic pockets on the protein instead (Figure 4.1B, C). In a "mattress model" of the membrane, which accounts for membrane stretch due to hydrophobic mismatch, such an extensive deviation would incur a large energy penalty due to "pulling" the lower leaflet tails away from the upper leaflet tails. Since the simulations reveal that this is not the case, we can ignore the bilayer compression term that couples the lower and upper leaflets. Third, we must include Gaussian curvature terms typically ignored in continuum membrane models, since the boundary curvature drastically changes between open and closed states (Figure 4.1A). The Gauss-Bonnet theorem states that the total Gaussian curvature, and hence the Gaussian bending energy, is a topological invariant; however, this is not true when the curvature or shape of the membrane changes along the boundary of the surface, which it does when the channel opens and closes. Finally, we ignore the relatively small deviations observed in the open state and assume that the open state has no associated membrane deformation energy. With these assumptions, the continuum model for the energy of a compressionless membrane is given by

$$G_M = \frac{1}{2}\int d\Omega \left\{ \frac{K_c}{2}\left(\nabla^2 u\right)^2 + \frac{T}{2}\left(\vec{\nabla} u\right)^2 \right\} \tag{4.1}$$

where dΩ is the membrane surface differential element, K_c is the bilayer mean bending modulus, T is the applied tension, and u is the deflection of the lower leaflet away from its equilibrium value along the z-axis. Taking the derivative of this energy functional, we arrive at a system of equations that govern the equilibrium shape of the membrane. We then solve the shape-dependent terms together, assuming an idealized radial symmetric constant offset and a far field boundary that is asymptotically flat, and add in the shape-independent Gaussian bending energy. The solutions are given by Equation 4.9 in the Methods, and the membrane dependent energy change for gating is

$$G_M = -\frac{1}{2}K_G\pi s^2 + \frac{\pi T^{\frac{3}{2}} r_0 u_0^2}{K_c^{\frac{1}{2}}} \frac{K_1 k r_0}{K_0 k r_0} \tag{4.2}$$

where K_G is the bilayer Gaussian bending modulus, r_0 is the radius at the inner boundary, u_0 is the deflection along the z-axis at the inner boundary, $k = \sqrt{T/K_c}$, and K_m are order m modified Bessel functions of the second kind. We note that the open state is stabilized by a $T^{3/2}$ term, meaning the model is even more sensitive to tension than the traditional area expansion models (Figure 4.2A). Super-linear tension dependence of membrane deformations has been reported before, and while the Bessel functions contribute some tension dependence beyond that of opening, regardless the scaling is greater than 1. Elastic membrane models typically involve 4 sets of boundary conditions (BCs), as they are solutions to 4th order equations. Generally, this involves 2 BCs on an inner boundary with a membrane protein, and 2 on an outer boundary far from the protein. Since we assume an asymptotically flat membrane infinitely far from the protein, this sets 3 BCs on the outer boundary leaving only one free parameter at the inner boundary – the deflection (u_0). Hence, the membrane energy above corresponds to solutions where the slopes at the inner boundary increase with added tension (Figure 4.2B).

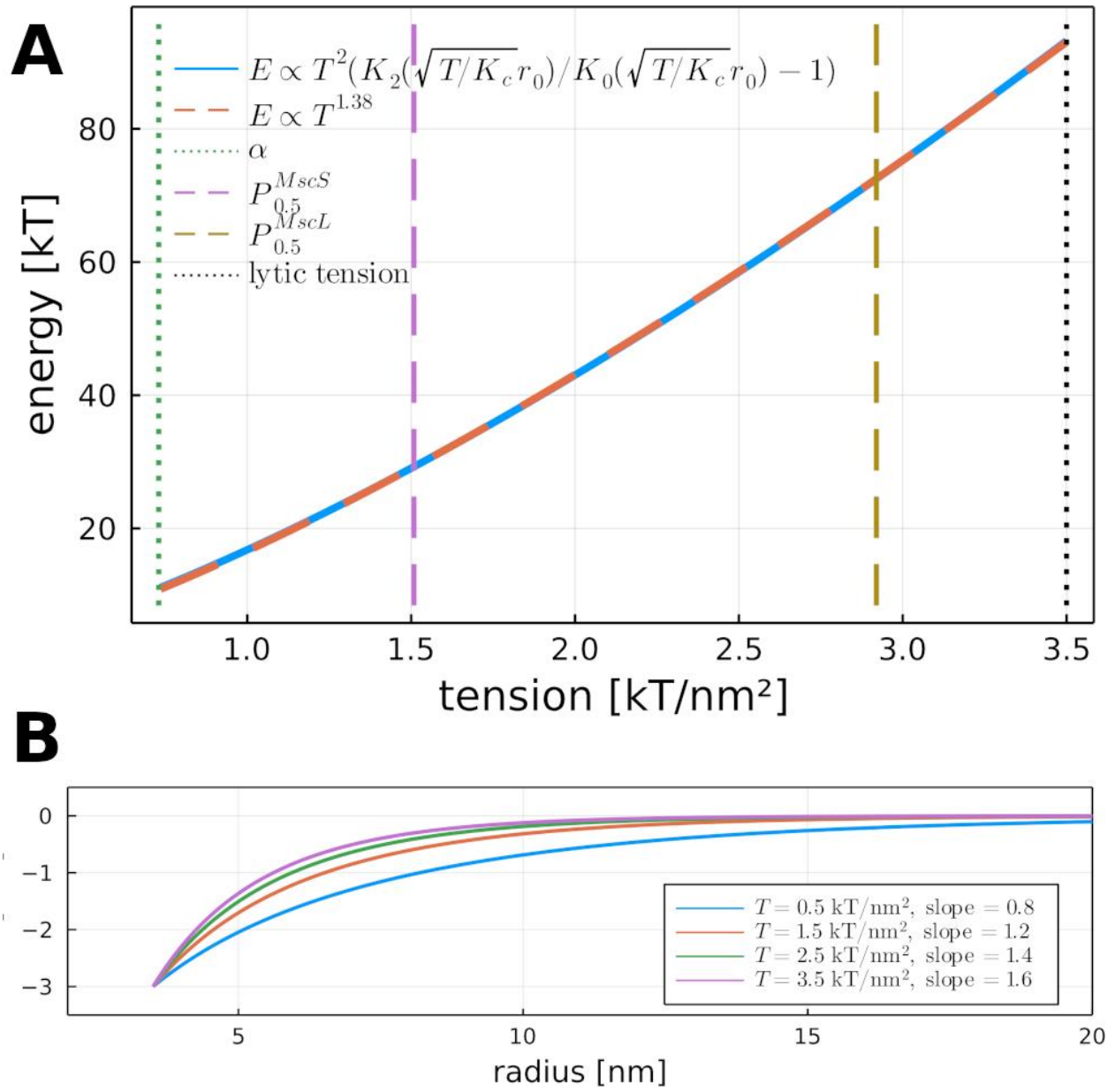

Figure 4.2 Analytical solutions of the continuum model.
(A) Free energy vs. applied tension, where the tension goes from stretch modulus to the lytic tension. The top (blue) line shows the equation for a single-leaflet deflection derived from Equation 4.12. The dashed line indicates that the energy dependence on tension is somewhere between linear and quadratic for the parameters used here. Also shown are the usual stretch modulus α, the tensions for 50% open probability for MscS and MscL, and the lytic tension. (B) Membrane deformation vs. tension in the compressionless model determined from Equation 4.12. The y axis is membrane height in nm. The slope is determined by the tension.

Coarse-grained simulations suggest the closed deformation is clamped. Next, we critically probed this idea that the membrane shape changes with applied tension, since it was previously observed that the distortion remained similar under different amounts of applied tension (Park et al.). Here, we took a different approach. Starting from a flat membrane build with well-packed lipids in the upper and lower leaflets, we expect that insertion of the closed state channel into the membrane followed by the extreme distortion in the lower leaflet results in a lower leaflet under very high tension and an upper leaflet under compression. Thus, we posited that even in the absence of an applied tension in the plane of the membrane the lower leaflet was under high tension. To relieve this strain, we took the closed state system, removed 10% of the lipids in the upper leaflet, and carried out an additional 10 μs of CGMD using this new asymmetric bilayer. When we compared the average membrane from the asymmetric system to the original system, we found no significant difference between the two (Figure 4.3).

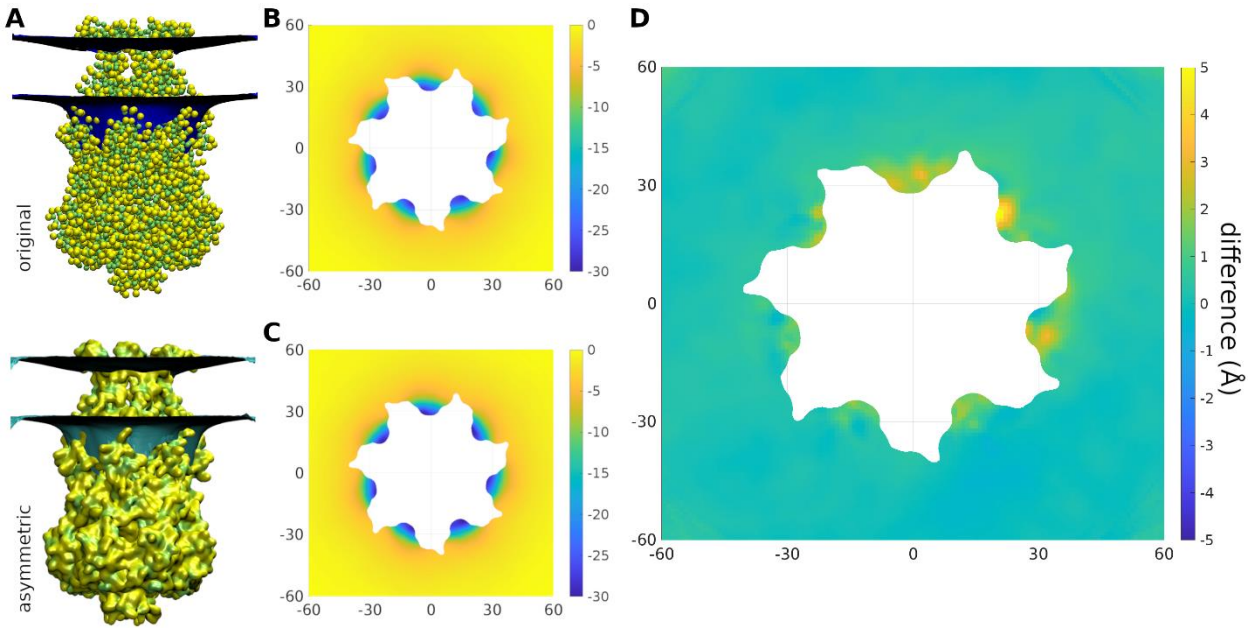

Figure 4.3 Few differences between original and asymmetric bilayer.
(A) Top: average membrane shape (blue) around closed MscS (yellow) as shown in Figure 4.1A. Bottom: average membrane shape (blue) around the same protein during a 10 μs simulation with asymmetric membrane. (B) The average lower leaflet surface around closed MscS as determined from 11 μs CGMD. Color scale represents membrane height (membrane is bending into the page.) Same data as Figure 4.1D. (C) Average lower leaflet surface from the asymmetric simulation. Same color scale as previous panel. (D) Difference between the two surfaces in panels B and C.

Thus, while these solutions nicely draw out the positive correlation between applied tension, induced curvature, and energy, they are not accurate representations of the protein-membrane system because the protein imposes both specific inner boundary conditions and specific contact angles at the membrane-protein contact curve.

Numeric solutions qualitatively reproduce the membrane shape. To model the membrane more correctly, we turned to our numeric membrane solver so that we could impose BCs and angles derived directly from the CGMD and generate more faithful solutions. These were extracted using level sets generated from the average MD surfaces and from an aligned copy of the protein structure, and seventh order Fourier coefficients were fit to the resulting BCs (Figure 4.1D). After plugging these in, we find that the resulting shape looks more like the average membrane from simulation, albeit with less of a sharp elbow shape (Figure 4.4). The energy-tension correlation is now linear instead of super-linear (Figure 4.5A), with relatively large energies that likely arise because we are dealing with a large deformation using the small angle approximation, which can artificially increase energy. We also note that the true membrane deformation energy of the open state is likely not zero, as we have assumed here. This may be because the membrane shape is fixed for a given value of applied tension, as observed in CGMD, which would make the shape term $\vec{\nabla}u$ in the energy constant leading $\frac{T}{2}(\vec{\nabla}u)^2$ to scale linearly with T.

Comparison to experimental data. Next, we wanted to compare the tension dependence of opening from our calculations to the experimental measurements of MscS opening in patch recordings by Nomura and company (Nomura et al.). To do this, we created a two-state model of opening and solved for the open state probability as a function of tension,

$$P_O(T) = \frac{1}{1+e^{\Delta G/k_B T}} \tag{4.3}$$

$$\Delta G = \Delta G_0 - \frac{1}{{\Delta G_0}^{n-1}} T^n \tag{4.4}$$

where $\Delta G_0 = G_O - G_C$ is the energy difference between the open and closed state, respectively, in the absence of tension, T is the applied tension, and n is the power of the tension dependence. The experimental data shows opening of MscS near 6.5 mN/m, so this equation opens when $\frac{\Delta G_0}{k_B T} = 6.5$, which constrains the prefactor in front of the tension. We plotted the open probability, as well as a prediction based on the continuum results that assumed channel opening depends linearly on tension (yellow curve, Figure 4.5B). As this was not a good fit, we also looked at the square of the tension (red curve) and the cube (blue curve) and found that channel opening probability is best modeled by an energy that scales like the cube of the tension (Figure 4.5B), as described by

$$P_o = \frac{1}{1+e^{6.5-\frac{1}{6.5^2 * T^3}}} \tag{4.5}$$

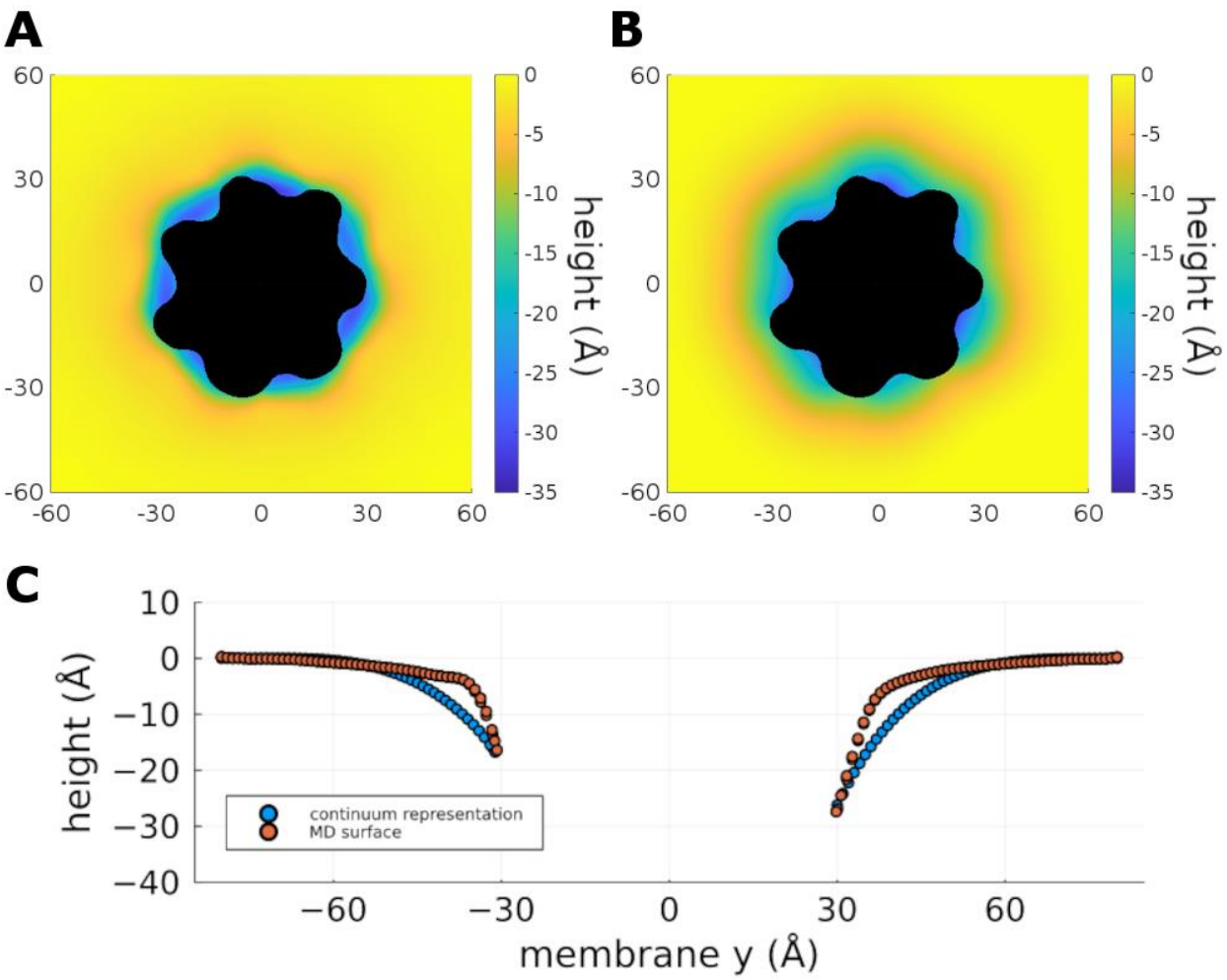

Figure 4.4 Comparison of membrane shape from CGMD versus continuum model. (A) The average lower leaflet surface around closed MscS as determined from 11 μs CGMD. Color scale represents membrane height (membrane bends into the page.) Same data as Figure 4.1D. (B) Average lower leaflet surface as represented by the continuum model. Same color scale as previous panel. (C) Slice through the membrane shapes in A and B along x=0. Different minimum heights on the left and right are due to the heptameric shape of the boundary.

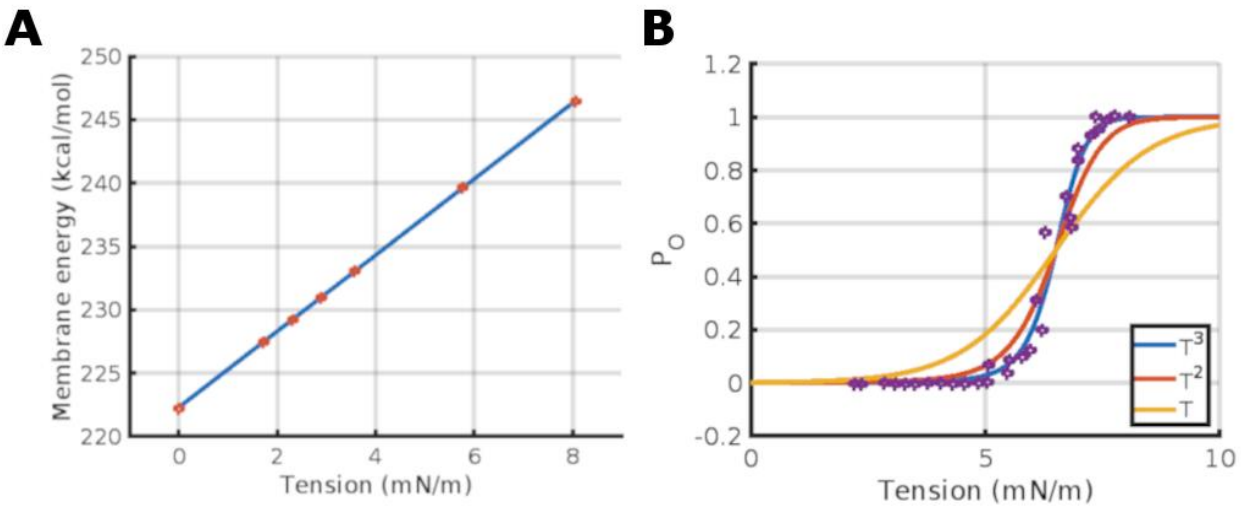

Figure 4.5 Channel behavior as a function of tension.
(A) Membrane energy as determined by the continuum model at various tensions, from 0 mN/m all the way to the lytic tension of 8.1 mN/m. Data points are in blue and linear fit is in red. (B) Channel opening probability versus applied tension, with data points in purple and idealized predictions as solid lines. $P_{0.5}$ is ~6.1 mN/m. Experimental data taken from (Nomura et al).

Re-imagining area expansion. Previous models have proposed that membrane energy arises from the product of tension and in-plane area change, and that the stability of the two-state system might arise from the balance between this tension product and the intrinsic energy of the closed versus open state of the protein (Wiggins and Phillips; Nomura et al.). In our present model we suggest two updates to this concept: first, we re-introduce the Gaussian bending energy term to account for the large curvature changes between states, and second, we re-define area expansion in terms of the curvature deformations. While there is no significant expansion of the protein in the plane parallel to the membrane, there is still expansion in the total surface area of the membrane that comes from stretching the membrane down to fill the hydrophobic pockets. Area expansion is accounted for in this model via the second term in the energy functional that scales linearly with tension $\frac{\mathrm{T}}{2}\left(\vec{\nabla}u\right)^2$. In the small angle limit, the gradient of u corresponds to the relative area expansion of a local patch of membrane, which when squared and multiplied by tension gives rise to an elastic energy term. The area change associated with the membrane shape in Figure 4.3 is approximately 21 nm^2. This is even larger than the in-plane area expansions reported for MscL of 6.5 nm^2 (Sukharev et al.). An area change of this size, going from 0 applied tension to the critical

tension of 1.5 kT/nm^2, would require ~15.8 kT of energy; this estimate does not include the Gaussian bending energy as we expect it to be constant when the protein does not change shape because the membrane boundary does not change. Curvature also increases with tension but attempts to increase curvature while maintaining fixed endpoints and contact angles will necessarily increase area. This could drive the positive correlation between tension, curvature, and area expansion in the continuum model. In the "membrane deformation" model, this would mean a dependence on membrane area expansion and curvature to generate a large positive membrane energy.

How is the high membrane energy of the closed state possible? It is offset by the energetic savings of the inserted protein. After plugging G_M back into a more complete continuum-atomistic model that also accounts for the energy of protein insertion via nonpolar (G_{np}) and electrostatic (G_{elec}) components (Marcoline et al.; Argudo, Bethel, Marcoline, Wolgemuth, et al.), we find that G_{np} = -848 kcal/mol and G_{elec} = 746 kcal/mol – thus the total energy for this system is 120 kcal/mol, or ~202 k_BT, a likely overestimation given that a completely flat upper bilayer would force some unfavorable arginine desolvations. Together, these findings support a two-state system that balances energetically favorable protein insertion and energetically unfavorable membrane deformation (Equation 4.4), where beyond the critical tension the positive energy component greatly outweighs the negative one and drives the channel to open.

$$G_{open} = \underbrace{G_M^{mean} + G_M^{Gaussian} + G_M^{tension} + G_{elec}}_{\text{positive}} + \underbrace{G_{np}}_{\text{negative}} \tag{4.6}$$

Future work will focus on improving the fit of the continuum model to the membrane shapes obtained with CGMD and continued efforts to describe the cubic tension relation to channel opening probability.

Materials and Methods

Molecular dynamics simulation

Coarse-grained MD (CGMD) simulations of the closed state (PDB ID 6PWP) and open state (PDB ID 8DDJ) of MscS were carried out for 11 μs and 10 μs, respectively, using MARTINI 2.2 (Marrink et al.) with elastic network dynamics (Periole et al.) in GROMACS 2018 (Abraham et al.), following the protocol described in Ref. (Park et al.). First, a POPC bilayer was generated with CHARMM-GUI (Lee, Cheng, et al.) using an initial box size of 170 x 170 x 180 $Å^3$, containing 847 lipids and 150 mM NaCl. Prior to adding protein, the POPC bilayer underwent 500,000 steps of steepest-descent minimization, three steps of equilibration with increasing tau_p, and 2 μs of unrestrained simulation as in Ref. (Park et al.). Afterward, the protein was placed into the box by aligning the transmembrane region (residues 21–44 and 80–89) with the bilayer, converted to coarse-grain representation using martinize2 and mkdssp 3.0 (Kabsch and Sander), and the corresponding topology files were updated. Each system contained only one copy of the protein. After addition of the protein, the system underwent 20,000 additional steps of minimization and four steps of equilibration with stepwise lowering of protein/lipid head restraints from 1000/200 to 250/20 kJ/(mol·nm^2), increasing the timestep and tau_p as in Ref. (Park et al). For all equilibration steps, a Berendsen barostat was used. For all production simulations, a 20 fs timestep and Parrinello-Rahman barostat were used, and a 250 kJ/(mol·nm^2) restraint was placed on the protein to ensure it did not stray excessively far from the starting coordinates. All equilibration and production simulations used a Verlet cut-off scheme with an 11 Å cut-off distance, semi-isotropic pressure coupling, the Reaction-field method for treating long-range electrostatic interactions, and in all cases, temperature was held at 303.15 K.

Membrane averaging

Membrane surface calculations were performed using a custom analysis package based on MDAnalysis (Michaud-Agrawal et al.; Gowers et al.), NumPy (Harris et al.), and SciPy (Virtanen et al.) with the same approach as outlined previously (Bethel and Grabe). To prepare the MD trajectories, we centered on the

protein, then rotationally and translationally (constrained to the XY-plane) fit to the protein using GROMACS (gmx trjconv) to maintain the starting configuration. To calculate, we erect a rectilinear grid with 1 Å spacing everywhere except at the protein-membrane interface, where we use a level set method based on the protein structure to move adjacent membrane grid points onto the surface (Argudo, Bethel, Marcoline, Wolgemuth, et al.). Then, we interpolate the positions of GL1 and GL2 beads (glycerol groups) on POPC residues from the CGMD onto this distorted grid using SciPy's implementation of the Clough-Tocher scheme to construct a hydrophobic surface for each leaflet at every time point analyzed. The midpoint of the bilayer was defined using the terminal hydrocarbon beads (C4A/C4B). A box size of 160 Å × 160 Å was used. All surfaces were then averaged across timepoints, and membrane profiles were visualized using MATLAB (R2023a) (MathWorks, Natick, MA, USA), Plots.jl (Breloff), and Julia (Bezanson et al.).

Continuum model

The elastic membrane energy is based on a Helfrich-Canham model of the lower leaflet of the bilayer.

$$G_M = \frac{1}{2}\int d\Omega \left\{\frac{K_c}{2}\left(\nabla^2 u\right)^2 + \frac{T}{2}\left(\vec{\nabla} u\right)^2\right\} \tag{4.7}$$

The Euler-Lagrange equations for this energy functional are then

$$\nabla^4 u - k^2\nabla^2 u = 0, \tag{4.8}$$

where $k = \sqrt{T/K_c}$. Solved in polar coordinates, it has the solutions

$$\mathrm{u}(r,\phi) = \mathrm{A} + \mathrm{D}\ln(r) + \sum_{m=0}^{\infty}\left[B_m I_m(kr)\cos\left(m(\phi+\delta_m^I)\right) + C_m K_m(kr)\cos\left(m(\phi+\delta_m^K)\right)\right] \tag{4.9}$$

where I_m and K_m are order m modified Bessel functions of the first and second kind, and A, D, B_m, C_m, δ_m^I, and δ_m^K are constants determined by the boundary conditions. Initially, we consider the cylindrically symmetric case, m = 0, which is asymptotically flat and goes to zero as r approaches infinity far from the protein with a constant downward deflection of magnitude $u(r_0) = u_0$ on the inner boundary r = r_0 where it touches the protein:

$$u(r_0) = u_0 = C_0 K_0(kr_0) \tag{4.10}$$

Finally, we assume that the slope of the membrane $\frac{\partial}{\partial r}u(r)$ at the point of contact with the protein is s such that $u'(r_0) = -u_0 k \frac{K_1(kr_0)}{K_0(kr_0)} = s$.

The total membrane elastic energy can be determined in two steps. First, the mean and tension dependent terms will be solved together as they both depend on the membrane shape in the solution domain, and second the Gaussian energy will be determined separately as it only depends on the solution at the boundary. Using $\nabla u = -ck\,K_1(kr)$ and $\nabla^2 u = ck^2\,K_0(kr)$, the energy is

$$G_M^{mean} + G_M^{tension} = \pi c^2 k^4 K_c \int_{r_0}^{\infty} dr\, r\{K_0^2(kr_0) + K_1^2(kr_0)\} \tag{4.11}$$

$$= \pi c^2 k^4 K_c \left\{\frac{1}{2} r_0^2 \left(K_1^2(kr_0) - K_0^2(kr_0)\right) + \frac{1}{2} r_0^2 \left(K_0(kr_0)K_2(kr_0) - K_1^2(kr_0)\right)\right\}$$

$$= \frac{1}{2}\pi c^2 k^4 K_c r_0^2 K_0(kr_0)\big(K_2(kr_0) - K_0(kr_0)\big)$$

$$= \frac{\pi c^2 T^2 r_0^2}{2K_c} K_0(kr_0)\big(K_2(kr_0) - K_0(kr_0)\big)$$

$$= \frac{\pi T^2 r_0^2 u_0^2}{2K_c}\left(\frac{K_2(kr_0)}{K_0(kr_0)} - 1\right)$$

or equivalently,

$$G_M^{mean} + G_M^{tension} = \frac{\pi T^{\frac{3}{2}} r_0 u_0^2}{K_c^{\frac{1}{2}}} \frac{K_1(kr_0)}{K_0(kr_0)}. \quad (4.12)$$

Hence, the membrane deformation energy in the closed state depends super-linearly on tension. There is still hidden tension dependence in the Bessel functions, but this energy ultimately scales like T^N where *N* is greater than 1 but less than 2. As discussed in the main text, this tension dependence on membrane deformations has been noted before.

We then re-introduce the Gaussian curvature energy term as the determinant of the second fundamental form divided by the determinant of the metric. By the divergence theorem, the surface integral of the Gaussian curvature can be converted to a boundary integral:

$$G_M^{Gauss} = \frac{K_G}{2} \int_{\partial\Omega} \left[\left(\overrightarrow{\nabla \vec{n}} \right) \vec{n} - \left(\vec{\nabla} \cdot \vec{n} \right) \vec{n} \right] \cdot \hat{s}\, dl \quad (4.13)$$

where ŝ is the direction normal to boundary. The integral is zero along the flat, far field boundary condition at infinity. At the protein-membrane contact, for a cylindrical boundary with constant offset and slope, $s = \nabla u \cdot \hat{s} = \frac{\partial u}{\partial r}$, this energy reduces to $G_M^{Gauss} = -\frac{1}{2} K_G \pi s^2$. Hence, when the membrane goes flat s = 0 as the channel opens, this term vanishes. Thus, the total membrane bending energy, as given in the main text, is:

$$G_M = -\frac{1}{2} K_G \pi s^2 + \frac{\pi T^{\frac{3}{2}} r_0 u_0^2}{K_c^{\frac{1}{2}}} \frac{K_1 kr_0}{K_0 kr_0} \quad (4.14)$$

The complete continuum-atomistic model developed by the Grabe lab is as previously described (Marcoline et al.; Argudo, Bethel, Marcoline, Wolgemuth, et al.) where the total free energy of the membrane-protein system is given by

$$\Delta G = G_{np} + G_{elec} + G_M \quad (4.15)$$

where G_{np} is the nonpolar energy associated with burying the protein surface area in the hydrophobic membrane environment, G_{elec} is the electrostatic energy required to place the protein in a low-dielectric environment, and G_M is the elastic membrane energy. This model has been shown to accurately predict the membrane deformation profile induced by several proteins including TMEM16 lipid scramblases (Bethel and Grabe) and small peptides such as gramicidin (Argudo, Bethel, Marcoline, Wolgemuth, et al.). The low-dielectric region is defined between two boundary surfaces representing the shape and height of the membrane hydrophobic region.

The numeric solutions shown in Figures 4.3 and 4.4 also include a compression scaling term that turns on compression like $1 - \left(1 \times \frac{1}{1+e^{-(D+10)}}\right)$, where D is the distance from the center of the grid.

5. REFERENCES

Abraham, Mark James, et al. “GROMACS: High Performance Molecular Simulations through Multi-Level Parallelism from Laptops to Supercomputers.” *SoftwareX*, vol. 1–2, Sept. 2015, pp. 19–25. *DOI.org (Crossref)*, https://doi.org/10.1016/j.softx.2015.06.001.

Adams, A., et al. *Methods in Yeast Genetics: A Cold Spring Harbor Laboratory Course Manual, 1997 Edition*. New York: Cold Spring Harbor Laboratory Press, 1998.

AMBER 2019. University of California, San Francisco, 2019.

Amberg, David C., et al. *Methods in Yeast Genetics: A Cold Spring Harbor Laboratory Course Manual*. 2005.

Åqvist, Johan, et al. “Molecular Dynamics Simulations of Water and Biomolecules with a Monte Carlo Constant Pressure Algorithm.” *Chemical Physics Letters*, vol. 384, no. 4–6, Jan. 2004, pp. 288–94. *DOI.org (Crossref)*, https://doi.org/10.1016/j.cplett.2003.12.039.

Argudo, David, Neville P. Bethel, Frank V. Marcoline, and Michael Grabe. “Continuum Descriptions of Membranes and Their Interaction with Proteins: Towards Chemically Accurate Models.” *Biochimica et Biophysica Acta (BBA) - Biomembranes*, vol. 1858, no. 7, July 2016, pp. 1619–34. *DOI.org (Crossref)*, https://doi.org/10.1016/j.bbamem.2016.02.003.

Argudo, David, Neville P. Bethel, Frank V. Marcoline, Charles W. Wolgemuth, et al. “New Continuum Approaches for Determining Protein-Induced Membrane Deformations.” *Biophysical Journal*, vol. 112, no. 10, May 2017, pp. 2159–72. *DOI.org (Crossref)*, https://doi.org/10.1016/j.bpj.2017.03.040.

Baeza-Delgado, Carlos, et al. “Structure-Based Statistical Analysis of Transmembrane Helices.” *European Biophysics Journal*, vol. 42, no. 2–3, Mar. 2013, pp. 199–207. *DOI.org (Crossref)*, https://doi.org/10.1007/s00249-012-0813-9.

Baker, Nathan A., et al. “Electrostatics of Nanosystems: Application to Microtubules and the Ribosome.” *Proceedings of the National Academy of Sciences*, vol. 98, no. 18, Aug. 2001, pp. 10037–41. *DOI.org (Crossref)*, https://doi.org/10.1073/pnas.181342398.

Bass, Randal B., et al. “Crystal Structure of *Escherichia Coli* MscS, a Voltage-Modulated and Mechanosensitive Channel.” *Science*, vol. 298, no. 5598, Nov. 2002, pp. 1582–87. *DOI.org (Crossref)*, https://doi.org/10.1126/science.1077945.

Berendsen, H. J. C., et al. “Molecular Dynamics with Coupling to an External Bath.” *The Journal of Chemical Physics*, vol. 81, no. 8, Oct. 1984, pp. 3684–90. *DOI.org (Crossref)*, https://doi.org/10.1063/1.448118.

Berner, Nicole, et al. “Protein Quality Control of the Endoplasmic Reticulum and Ubiquitin–Proteasome-Triggered Degradation of Aberrant Proteins: Yeast Pioneers the Path.” *Annual Review of Biochemistry*, vol. 87, no. 1, June 2018, pp. 751–82. *DOI.org (Crossref)*, https://doi.org/10.1146/annurev-biochem-062917-012749.

Bethel, Neville P., and Michael Grabe. “Atomistic Insight into Lipid Translocation by a TMEM16 Scramblase.” *Proceedings of the National Academy of Sciences*, vol. 113, no. 49, Dec. 2016, pp. 14049–54. *Crossref*, https://doi.org/10.1073/pnas.1607574113.

Bezanson, Jeff, et al. “Julia: A Fresh Approach to Numerical Computing.” *SIAM Review*, vol. 59, no. 1, Jan. 2017, pp. 65–98. *DOI.org (Crossref)*, https://doi.org/10.1137/141000671.

Bichet, Daniel G., et al. “Aquaporin-2: New Mutations Responsible for Autosomal-Recessive Nephrogenic Diabetes Insipidus-Update and Epidemiology.” *Clinical Kidney Journal*, vol. 5, no. 3, June 2012, pp. 195–202. *PubMed*, https://doi.org/10.1093/ckj/sfs029.

Brambilla Pisoni, Giorgia, and Maurizio Molinari. “Five Questions (with Their Answers) on ER-Associated Degradation: Endoplasmic Reticulum-Associated Degradation.” *Traffic*, vol. 17, no. 4, Apr. 2016, pp. 341–50. *DOI.org (Crossref)*, https://doi.org/10.1111/tra.12373.

Breloff, Tom. *Plots.Jl*. v1.38.17, Zenodo, 25 July 2023. *DOI.org (Datacite)*, https://doi.org/10.5281/ZENODO.4725317.

Brodsky, J. L., and R. Schekman. “A Sec63p-BiP Complex from Yeast Is Required for Protein Translocation in a Reconstituted Proteoliposome.” *The Journal of Cell Biology*, vol. 123, no. 6, Dec. 1993, pp. 1355–63. *DOI.org (Crossref)*, https://doi.org/10.1083/jcb.123.6.1355.

Buck, Teresa M., et al. “A Novel Tripartite Motif Involved in Aquaporin Topogenesis, Monomer Folding and Tetramerization.” *Nature Structural & Molecular Biology*, vol. 14, no. 8, Aug. 2007, pp. 762–69. *DOI.org (Crossref)*, https://doi.org/10.1038/nsmb1275.

Buck, Teresa M., and William R. Skach. “Differential Stability of Biogenesis Intermediates Reveals a Common Pathway for Aquaporin-1 Topological Maturation.” *Journal of Biological Chemistry*, vol. 280, no. 1, Jan. 2005, pp. 261–69. *DOI.org (Crossref)*, https://doi.org/10.1074/jbc.M409920200.

Cao, Zheng, et al. “Backbone Hydrogen Bond Strengths Can Vary Widely in Transmembrane Helices.” *Journal of the American Chemical Society*, vol. 139, no. 31, Aug. 2017, pp. 10742–49. *DOI.org (Crossref)*, https://doi.org/10.1021/jacs.7b04819.

Carveth, Kristin, et al. “Cooperativity and Flexibility of Cystic Fibrosis Transmembrane Conductance Regulator Transmembrane Segments Participate in Membrane Localization of a Charged Residue.” *The Journal of Biological Chemistry*, vol. 277, no. 42, Oct. 2002, pp. 39507–14. *PubMed*, https://doi.org/10.1074/jbc.M205759200.

Chang, Geoffrey, et al. “Structure of the MscL Homolog from *Mycobacterium Tuberculosis* : A Gated Mechanosensitive Ion Channel.” *Science*, vol. 282, no. 5397, Dec. 1998, pp. 2220–26. *DOI.org (Crossref)*, https://doi.org/10.1126/science.282.5397.2220.

Cheng, Seng H., et al. “Defective Intracellular Transport and Processing of CFTR Is the Molecular Basis of Most Cystic Fibrosis.” *Cell*, vol. 63, no. 4, Nov. 1990, pp. 827–34. *DOI.org (Crossref)*, https://doi.org/10.1016/0092-8674(90)90148-8.

Christianson, John C., and Yihong Ye. “Cleaning up in the Endoplasmic Reticulum: Ubiquitin in Charge.” *Nature Structural & Molecular Biology*, vol. 21, no. 4, Apr. 2014, pp. 325–35. *DOI.org (Crossref)*, https://doi.org/10.1038/nsmb.2793.

Cordes, Frank S., et al. “Proline-Induced Distortions of Transmembrane Helices.” *Journal of Molecular Biology*, vol. 323, no. 5, Nov. 2002, pp. 951–60. *DOI.org (Crossref)*, https://doi.org/10.1016/S0022-2836(02)01006-9.

Cox, Charles D., et al. “Bacterial Mechanosensors.” *Annual Review of Physiology*, vol. 80, no. 1, Feb. 2018, pp. 71–93. *DOI.org (Crossref)*, https://doi.org/10.1146/annurev-physiol-021317-121351.

Cui, Guiying, et al. “Mutations at Arginine 352 Alter the Pore Architecture of CFTR.” *The Journal of Membrane Biology*, vol. 222, no. 2, Mar. 2008, pp. 91–106. *PubMed*, https://doi.org/10.1007/s00232-008-9105-9.

Cymer, Florian, et al. “Mechanisms of Integral Membrane Protein Insertion and Folding.” *Journal of Molecular Biology*, vol. 427, no. 5, Mar. 2015, pp. 999–1022. *DOI.org (Crossref)*, https://doi.org/10.1016/j.jmb.2014.09.014.

Dahl, A. C. E., et al. “Bendix: Intuitive Helix Geometry Analysis and Abstraction.” *Bioinformatics*, vol. 28, no. 16, Aug. 2012, pp. 2193–94. *Crossref*, https://doi.org/10.1093/bioinformatics/bts357.

Darden, Tom, et al. “Particle Mesh Ewald: An $N \cdot \log(N)$ Method for Ewald Sums in Large Systems.” *The Journal of Chemical Physics*, vol. 98, no. 12, June 1993, pp. 10089–92. *DOI.org (Crossref)*, https://doi.org/10.1063/1.464397.

Decottignies, Anabelle, and André Goffeau. “Complete Inventory of the Yeast ABC Proteins.” *Nature Genetics*, vol. 15, no. 2, Feb. 1997, pp. 137–45. *DOI.org (Crossref)*, https://doi.org/10.1038/ng0297-137.

Dickson, Callum J., et al. “Lipid14: The Amber Lipid Force Field.” *Journal of Chemical Theory and Computation*, vol. 10, no. 2, Feb. 2014, pp. 865–79. *DOI.org (Crossref)*, https://doi.org/10.1021/ct4010307.

Dolinsky, T. J., et al. “PDB2PQR: An Automated Pipeline for the Setup of Poisson-Boltzmann Electrostatics Calculations.” *Nucleic Acids Research*, vol. 32, no. Web Server, July 2004, pp. W665–67. *DOI.org (Crossref)*, https://doi.org/10.1093/nar/gkh381.

Eastman, Peter, et al. “OpenMM 7: Rapid Development of High Performance Algorithms for Molecular Dynamics.” *PLOS Computational Biology*, edited by Robert Gentleman, vol. 13, no. 7, July 2017, p. e1005659. *DOI.org (Crossref)*, https://doi.org/10.1371/journal.pcbi.1005659.

Enquist, Karl, et al. “Membrane-Integration Characteristics of Two ABC Transporters, CFTR and P-Glycoprotein.” *Journal of Molecular Biology*, vol. 387, no. 5, Apr. 2009, pp. 1153–64. *PubMed*, https://doi.org/10.1016/j.jmb.2009.02.035.

Feige, Matthias J., and Linda M. Hendershot. “Quality Control of Integral Membrane Proteins by Assembly-Dependent Membrane Integration.” *Molecular Cell*, vol. 51, no. 3, Aug. 2013, pp. 297–309. *PubMed*, https://doi.org/10.1016/j.molcel.2013.07.013.

Gaczynska, Maria, and Pawel A. Osmulski. “Small-Molecule Inhibitors of Proteasome Activity.” *Ubiquitin-Proteasome Protocols*, by Cam Patterson and Douglas M. Cyr, vol. 301, Humana Press, 2005, pp. 003–22. *DOI.org (Crossref)*, https://doi.org/10.1385/1-59259-895-1:003.

Geller, Dorit, et al. “Comparative Topology Studies in Saccharomyces Cerevisiae and in Escherichia Coli.” *Journal of Biological Chemistry*, vol. 271, no. 23, June 1996, pp. 13746–53. *DOI.org (Crossref)*, https://doi.org/10.1074/jbc.271.23.13746.

Gomez, Yessica K., et al. “Taking the Monte-Carlo Gamble: How Not to Buckle under the Pressure!” *Journal of Computational Chemistry*, Dec. 2021, p. jcc.26798. *DOI.org (Crossref)*, https://doi.org/10.1002/jcc.26798.

Gowers, Richard, et al. *MDAnalysis: A Python Package for the Rapid Analysis of Molecular Dynamics Simulations*. 2016, pp. 98–105. *DOI.org (Crossref)*, https://doi.org/10.25080/Majora-629e541a-00e.

Guerriero, Christopher J., Yessica K. Gomez, et al. “Harmonizing Experimental Data with Modeling to Predict Membrane Protein Insertion in Yeast.” *Biophysical Journal*, vol. 117, no. 4, July 2019, pp. 668–78. *DOI.org (Crossref)*, https://doi.org/10.1016/j.bpj.2019.07.013.

Guerriero, Christopher J., Kurt F. Weiberth, et al. “Hsp70 Targets a Cytoplasmic Quality Control Substrate to the San1p Ubiquitin Ligase.” *Journal of Biological Chemistry*, vol. 288, no. 25, June 2013, pp. 18506–20. *DOI.org (Crossref)*, https://doi.org/10.1074/jbc.M113.475905.

Guerriero, Christopher J., Karl-Richard Reutter, et al. “Transmembrane Helix Hydrophobicity Is an Energetic Barrier during the Retrotranslocation of Integral Membrane ERAD Substrates.”

Molecular Biology of the Cell, edited by Anne Spang, vol. 28, no. 15, July 2017, pp. 2076–90. *Crossref*, https://doi.org/10.1091/mbc.e17-03-0184.

Guerriero, Christopher J., and Jeffrey L. Brodsky. "The Delicate Balance Between Secreted Protein Folding and Endoplasmic Reticulum-Associated Degradation in Human Physiology." *Physiological Reviews*, vol. 92, no. 2, Apr. 2012, pp. 537–76. *DOI.org (Crossref)*, https://doi.org/10.1152/physrev.00027.2011.

Hämmerle, M. M., et al. "Disease-Associated Mutations in the Extracytoplasmic Loops of Cystic Fibrosis Transmembrane Conductance Regulator Do Not Impede Biosynthetic Processing but Impair Chloride Channel Stability." *The Journal of Biological Chemistry*, vol. 276, no. 18, May 2001, pp. 14848–54. *PubMed*, https://doi.org/10.1074/jbc.M011017200.

Hampton, Randolph Y., and Thomas Sommer. "Finding the Will and the Way of ERAD Substrate Retrotranslocation." *Current Opinion in Cell Biology*, vol. 24, no. 4, Aug. 2012, pp. 460–66. *DOI.org (Crossref)*, https://doi.org/10.1016/j.ceb.2012.05.010.

Hanwell, Marcus D., et al. "Avogadro: An Advanced Semantic Chemical Editor, Visualization, and Analysis Platform." *Journal of Cheminformatics*, vol. 4, no. 1, Dec. 2012, p. 17. *DOI.org (Crossref)*, https://doi.org/10.1186/1758-2946-4-17.

Harris, Charles R., et al. "Array Programming with NumPy." *Nature*, vol. 585, no. 7825, Sept. 2020, pp. 357–62. *DOI.org (Crossref)*, https://doi.org/10.1038/s41586-020-2649-2.

Harroun, Thad A., et al. "Experimental Evidence for Hydrophobic Matching and Membrane-Mediated Interactions in Lipid Bilayers Containing Gramicidin." *Biophysical Journal*, vol. 76, no. 2, Feb. 1999, pp. 937–45. *DOI.org (Crossref)*, https://doi.org/10.1016/S0006-3495(99)77257-7.

Hedin, Linnea E., et al. "Membrane Insertion of Marginally Hydrophobic Transmembrane Helices Depends on Sequence Context." *Journal of Molecular Biology*, vol. 396, no. 1, Feb. 2010, pp. 221–29. *DOI.org (Crossref)*, https://doi.org/10.1016/j.jmb.2009.11.036.

Helfrich, W. “Elastic Properties of Lipid Bilayers: Theory and Possible Experiments.” *Zeitschrift Für Naturforschung C*, vol. 28, no. 11–12, Dec. 1973, pp. 693–703. *DOI.org (Crossref)*, https://doi.org/10.1515/znc-1973-11-1209.

Hess, Berk, et al. “LINCS: A Linear Constraint Solver for Molecular Simulations.” *Journal of Computational Chemistry*, vol. 18, no. 12, Sept. 1997, pp. 1463–72. *DOI.org (Crossref)*, https://doi.org/10.1002/(SICI)1096-987X(199709)18:12<1463::AID-JCC4>3.0.CO;2-H.

Hessa, Tara, Nadja M. Meindl-Beinker, et al. “Molecular Code for Transmembrane-Helix Recognition by the Sec61 Translocon.” *Nature*, vol. 450, Dec. 2007, p. 1026.

Hessa, Tara, Hyun Kim, et al. “Recognition of Transmembrane Helices by the Endoplasmic Reticulum Translocon.” *Nature*, vol. 433, no. 7024, Jan. 2005, pp. 377–81, https://doi.org/10.1038/nature03216.

Hill, Rose Z., et al. “PIEZO1 Transduces Mechanical Itch in Mice.” *Nature*, vol. 607, no. 7917, July 2022, pp. 104–10. *DOI.org (Crossref)*, https://doi.org/10.1038/s41586-022-04860-5.

Huang, Jing, and Alexander D. MacKerell. “CHARMM36 All-Atom Additive Protein Force Field: Validation Based on Comparison to NMR Data.” *Journal of Computational Chemistry*, vol. 34, no. 25, Sept. 2013, pp. 2135–45. *DOI.org (Crossref)*, https://doi.org/10.1002/jcc.23354.

Illing, Michelle E., et al. “A Rhodopsin Mutant Linked to Autosomal Dominant Retinitis Pigmentosa Is Prone to Aggregate and Interacts with the Ubiquitin Proteasome System.” *The Journal of Biological Chemistry*, vol. 277, no. 37, Sept. 2002, pp. 34150–60. *PubMed*, https://doi.org/10.1074/jbc.M204955200.

Jin, Peng, et al. “Electron Cryo-Microscopy Structure of the Mechanotransduction Channel NOMPC.” *Nature*, vol. 547, no. 7661, July 2017, pp. 118–22. *DOI.org (Crossref)*, https://doi.org/10.1038/nature22981.

Jo, Sunhwan, et al. “CHARMM-GUI: A Web-Based Graphical User Interface for CHARMM.” *Journal of Computational Chemistry*, vol. 29, no. 11, Aug. 2008, pp. 1859–65. *DOI.org (Crossref)*, https://doi.org/10.1002/jcc.20945.

Jorgensen, William L., et al. “Comparison of Simple Potential Functions for Simulating Liquid Water.” *The Journal of Chemical Physics*, vol. 79, no. 2, July 1983, pp. 926–35. *DOI.org (Crossref)*, https://doi.org/10.1063/1.445869.

Joung, In Suk, and Thomas E. Cheatham. “Determination of Alkali and Halide Monovalent Ion Parameters for Use in Explicitly Solvated Biomolecular Simulations.” *The Journal of Physical Chemistry B*, vol. 112, no. 30, July 2008, pp. 9020–41. *DOI.org (Crossref)*, https://doi.org/10.1021/jp8001614.

Junne, Tina, et al. “The Hydrophobic Core of the Sec61 Translocon Defines the Hydrophobicity Threshold for Membrane Integration.” *Molecular Biology of the Cell*, edited by Reid Gilmore, vol. 21, no. 10, May 2010, pp. 1662–70. *DOI.org (Crossref)*, https://doi.org/10.1091/mbc.e10-01-0060.

Junne, Tina, and Martin Spiess. “Integration of Transmembrane Domains Is Regulated by Their Downstream Sequences.” *Journal of Cell Science*, vol. 130, no. 2, Jan. 2017, pp. 372–81. *PubMed*, https://doi.org/10.1242/jcs.194472.

Kabsch, Wolfgang, and Christian Sander. “Dictionary of Protein Secondary Structure: Pattern Recognition of Hydrogen-Bonded and Geometrical Features.” *Biopolymers*, vol. 22, no. 12, Dec. 1983, pp. 2577–637. *DOI.org (Crossref)*, https://doi.org/10.1002/bip.360221211.

Kalienkova, Valeria, et al. “Stepwise Activation Mechanism of the Scramblase NhTMEM16 Revealed by Cryo-EM.” *ELife*, vol. 8, 2019, p. e44364.

Kefauver, J. M., et al. “Discoveries in Structure and Physiology of Mechanically Activated Ion Channels.” *Nature*, vol. 587, no. 7835, Nov. 2020, pp. 567–76. *DOI.org (Crossref)*, https://doi.org/10.1038/s41586-020-2933-1.

Klauda, Jeffery B., et al. “Update of the CHARMM All-Atom Additive Force Field for Lipids: Validation on Six Lipid Types.” *The Journal of Physical Chemistry B*, vol. 114, no. 23, June 2010, pp. 7830–43. *DOI.org (Crossref)*, https://doi.org/10.1021/jp101759q.

Kučerka, Norbert, et al. “Structure of Fully Hydrated Fluid Phase Lipid Bilayers with Monounsaturated Chains.” *Journal of Membrane Biology*, vol. 208, no. 3, Jan. 2006, pp. 193–202. *DOI.org (Crossref)*, https://doi.org/10.1007/s00232-005-7006-8.

Kuchler, K., et al. “Saccharomyces Cerevisiae STE6 Gene Product: A Novel Pathway for Protein Export in Eukaryotic Cells.” *The EMBO Journal*, vol. 8, no. 13, Dec. 1989, pp. 3973–84. *DOI.org (Crossref)*, https://doi.org/10.1002/j.1460-2075.1989.tb08580.x.

Lee, Do Hee, and Alfred L. Goldberg. “Selective Inhibitors of the Proteasome-Dependent and Vacuolar Pathways of Protein Degradation in Saccharomyces Cerevisiae.” *Journal of Biological Chemistry*, vol. 271, no. 44, Nov. 1996, pp. 27280–84. *DOI.org (Crossref)*, https://doi.org/10.1074/jbc.271.44.27280.

Lee, Jumin, Xi Cheng, et al. “CHARMM-GUI Input Generator for NAMD, GROMACS, AMBER, OpenMM, and CHARMM/OpenMM Simulations Using the CHARMM36 Additive Force Field.” *Journal of Chemical Theory and Computation*, vol. 12, no. 1, Jan. 2016, pp. 405–13. *DOI.org (Crossref)*, https://doi.org/10.1021/acs.jctc.5b00935.

Lee, Jumin, Manuel Hitzenberger, et al. “CHARMM-GUI Supports the Amber Force Fields.” *The Journal of Chemical Physics*, vol. 153, no. 3, July 2020, p. 035103. *DOI.org (Crossref)*, https://doi.org/10.1063/5.0012280.

Lerch-Bader, Mirjam, et al. “Contribution of Positively Charged Flanking Residues to the Insertion of Transmembrane Helices into the Endoplasmic Reticulum.” *Proceedings of the National Academy of Sciences*, vol. 105, no. 11, Mar. 2008, pp. 4127–32. *DOI.org (Crossref)*, https://doi.org/10.1073/pnas.0711580105.

Levina, N. “Protection of Escherichia Coli Cells against Extreme Turgor by Activation of MscS and MscL Mechanosensitive Channels: Identification of Genes Required for MscS Activity.” *The EMBO Journal*, vol. 18, no. 7, Apr. 1999, pp. 1730–37. *DOI.org (Crossref)*, https://doi.org/10.1093/emboj/18.7.1730.

Liu, Li-Ping, et al. “Threshold Hydrophobicity Dictates Helical Conformations of Peptides in Membrane Environments.” *Biopolymers*, vol. 39, no. 3, Feb. 1996, pp. 465–70. *DOI.org (Crossref)*, https://doi.org/10.1002/(SICI)1097-0282(199609)39:3<465::AID-BIP17>3.0.CO;2-A.

Loayza, Diego, et al. “Ste6p Mutants Defective in Exit from the Endoplasmic Reticulum (ER) Reveal Aspects of an ER Quality Control Pathway in Saccharomyces Cerevisiae.” *Molecular Biology of the Cell*, edited by Peter Walter, vol. 9, no. 10, Oct. 1998, pp. 2767–84. *DOI.org (Crossref)*, https://doi.org/10.1091/mbc.9.10.2767.

Lundin, Carolina, et al. “Molecular Code for Protein Insertion in the Endoplasmic Reticulum Membrane Is Similar for N_{in} –C_{out} and N_{out} –C_{in} Transmembrane Helices.” *Proceedings of the National Academy of Sciences*, vol. 105, no. 41, Oct. 2008, pp. 15702–07. *DOI.org (Crossref)*, https://doi.org/10.1073/pnas.0804842105.

MacCallum, Justin L., et al. “Partitioning of Amino Acid Side Chains into Lipid Bilayers: Results from Computer Simulations and Comparison to Experiment.” *The Journal of General Physiology*, vol. 129, no. 5, May 2007, pp. 371–77. *DOI.org (Crossref)*, https://doi.org/10.1085/jgp.200709745.

Marcoline, Frank V., et al. “Membrane Protein Properties Revealed through Data-Rich Electrostatics Calculations.” *Structure*, vol. 23, no. 8, Aug. 2015, pp. 1526–37. *Crossref*, https://doi.org/10.1016/j.str.2015.05.014.

Marrink, Siewert J., et al. “The MARTINI Force Field: Coarse Grained Model for Biomolecular Simulations.” *The Journal of Physical Chemistry B*, vol. 111, no. 27, July 2007, pp. 7812–24. *DOI.org (Crossref)*, https://doi.org/10.1021/jp071097f.

McGrath, John P., and Alexander Varshavsky. “The Yeast STE6 Gene Encodes a Homologue of the Mammalian Multidrug Resistance P-Glycoprotein.” *Nature*, vol. 340, no. 6232, Aug. 1989, pp. 400–04. *DOI.org (Crossref)*, https://doi.org/10.1038/340400a0.

Meindl-Beinker, Nadja M., et al. “Asn- and Asp-mediated Interactions between Transmembrane Helices during Translocon-mediated Membrane Protein Assembly.” *EMBO Reports*, vol. 7, no. 11, Nov. 2006, pp. 1111–16. *DOI.org (Crossref)*, https://doi.org/10.1038/sj.embor.7400818.

Michaud-Agrawal, Naveen, et al. “MDAnalysis: A Toolkit for the Analysis of Molecular Dynamics Simulations.” *Journal of Computational Chemistry*, vol. 32, no. 10, July 2011, pp. 2319–27. *DOI.org (Crossref)*, https://doi.org/10.1002/jcc.21787.

Milo, Ron, et al. “BioNumbers—the Database of Key Numbers in Molecular and Cell Biology.” *Nucleic Acids Research*, vol. 38, no. suppl_1, Jan. 2010, pp. D750–53. *DOI.org (Crossref)*, https://doi.org/10.1093/nar/gkp889.

Miyamoto, Shuichi, and Peter A. Kollman. “Settle: An Analytical Version of the SHAKE and RATTLE Algorithm for Rigid Water Models.” *Journal of Computational Chemistry*, vol. 13, no. 8, Oct. 1992, pp. 952–62. *DOI.org (Crossref)*, https://doi.org/10.1002/jcc.540130805.

Moon, C. Preston, and Karen G. Fleming. “Side-Chain Hydrophobicity Scale Derived from Transmembrane Protein Folding into Lipid Bilayers.” *Proceedings of the National Academy of Sciences*, vol. 108, no. 25, June 2011, p. 10174, https://doi.org/10.1073/pnas.1103979108.

Mulhall, Eric M., et al. “Direct Observation of the Conformational States of PIEZO1.” *Nature*, Aug. 2023. *DOI.org (Crossref)*, https://doi.org/10.1038/s41586-023-06427-4.

Nakatsukasa, Kunio, et al. “Dissecting the ER-Associated Degradation of a Misfolded Polytopic Membrane Protein.” *Cell*, vol. 132, no. 1, Jan. 2008, pp. 101–12. *DOI.org (Crossref)*, https://doi.org/10.1016/j.cell.2007.11.023.

Natale, Andrew M., et al. “Structural Insights into the Mechanisms and Pharmacology of K2P Potassium Channels.” *Journal of Molecular Biology*, vol. 433, no. 17, Aug. 2021, p. 166995. *DOI.org (Crossref)*, https://doi.org/10.1016/j.jmb.2021.166995.

Nilsson, I. M., and G. von Heijne. “Determination of the Distance between the Oligosaccharyltransferase Active Site and the Endoplasmic Reticulum Membrane.” *The Journal of Biological Chemistry*, vol. 268, no. 8, Mar. 1993, pp. 5798–801.

Nomura, Takeshi, et al. “Differential Effects of Lipids and Lyso-Lipids on the Mechanosensitivity of the Mechanosensitive Channels MscL and MscS.” *Proceedings of the National Academy of Sciences*,

vol. 109, no. 22, May 2012, pp. 8770–75. *DOI.org (Crossref)*, https://doi.org/10.1073/pnas.1200051109.

Öjemalm, Karin, et al. "Orientational Preferences of Neighboring Helices Can Drive ER Insertion of a Marginally Hydrophobic Transmembrane Helix." *Molecular Cell*, vol. 45, no. 4, Feb. 2012, pp. 529–40. *DOI.org (Crossref)*, https://doi.org/10.1016/j.molcel.2011.12.024.

Olzmann, J. A., et al. "The Mammalian Endoplasmic Reticulum-Associated Degradation System." *Cold Spring Harbor Perspectives in Biology*, vol. 5, no. 9, Sept. 2013, pp. a013185–a013185. *DOI.org (Crossref)*, https://doi.org/10.1101/cshperspect.a013185.

Overington, John P., et al. "How Many Drug Targets Are There?" *Nature Reviews Drug Discovery*, vol. 5, no. 12, Dec. 2006, pp. 993–96. *DOI.org (Crossref)*, https://doi.org/10.1038/nrd2199.

Park, Yein Christina, et al. "State-Specific Morphological Deformations of the Lipid Bilayer Explain Mechanosensitive Gating of MscS Ion Channels." *ELife*, vol. 12, Jan. 2023, p. e81445. *DOI.org (Crossref)*, https://doi.org/10.7554/eLife.81445.

Parrinello, M., and A. Rahman. "Polymorphic Transitions in Single Crystals: A New Molecular Dynamics Method." *Journal of Applied Physics*, vol. 52, no. 12, Dec. 1981, pp. 7182–90. *DOI.org (Crossref)*, https://doi.org/10.1063/1.328693.

Patrick, Anna E., et al. "Alteration of CFTR Transmembrane Span Integration by Disease-Causing Mutations." *Molecular Biology of the Cell*, vol. 22, no. 23, Dec. 2011, pp. 4461–71. *PubMed*, https://doi.org/10.1091/mbc.E11-05-0396.

Periole, Xavier, et al. "Combining an Elastic Network With a Coarse-Grained Molecular Force Field: Structure, Dynamics, and Intermolecular Recognition." *Journal of Chemical Theory and Computation*, vol. 5, no. 9, Sept. 2009, pp. 2531–43. *DOI.org (Crossref)*, https://doi.org/10.1021/ct9002114.

Perozo, Eduardo, D. Marien Cortes, et al. "Open Channel Structure of MscL and the Gating Mechanism of Mechanosensitive Channels." *Nature*, vol. 418, no. 6901, Aug. 2002, pp. 942–48. *DOI.org (Crossref)*, https://doi.org/10.1038/nature00992.

Perozo, Eduardo, Anna Kloda, et al. “Physical Principles Underlying the Transduction of Bilayer Deformation Forces during Mechanosensitive Channel Gating.” *Nature Structural Biology*, vol. 9, no. 9, Sept. 2002, pp. 696–703. *DOI.org (Crossref)*, https://doi.org/10.1038/nsb827.

Rapoport, Tom A., et al. “Structural and Mechanistic Insights into Protein Translocation.” *Annual Review of Cell and Developmental Biology*, vol. 33, no. 1, Oct. 2017, pp. 369–90. *DOI.org (Crossref)*, https://doi.org/10.1146/annurev-cellbio-100616-060439.

Reddy, Bharat, et al. “Molecular Basis of Force-from-Lipids Gating in the Mechanosensitive Channel MscS.” *ELife*, vol. 8, Dec. 2019, p. e50486. *DOI.org (Crossref)*, https://doi.org/10.7554/eLife.50486.

Roushar, Francis J., et al. “Contribution of Cotranslational Folding Defects to Membrane Protein Homeostasis.” *Journal of the American Chemical Society*, vol. 141, no. 1, Jan. 2019, pp. 204–15. *DOI.org (Crossref)*, https://doi.org/10.1021/jacs.8b08243.

Ryckaert, Jean-Paul, et al. “Numerical Integration of the Cartesian Equations of Motion of a System with Constraints: Molecular Dynamics of n-Alkanes.” *Journal of Computational Physics*, vol. 23, no. 3, Mar. 1977, pp. 327–41. *DOI.org (Crossref)*, https://doi.org/10.1016/0021-9991(77)90098-5.

Saaf, Annika, et al. “Stop-Transfer Function of Pseudo-Random Amino Acid Segments during Translocation across Prokaryotic and Eukaryotic Membranes.” *European Journal of Biochemistry*, vol. 251, no. 3, Feb. 1998, pp. 821–29. *DOI.org (Crossref)*, https://doi.org/10.1046/j.1432-1327.1998.2510821.x.

Sanner, Michel F., et al. “Reduced Surface: An Efficient Way to Compute Molecular Surfaces.” *Biopolymers*, vol. 38, no. 3, Mar. 1996, pp. 305–20. *DOI.org (Crossref)*, https://doi.org/10.1002/(SICI)1097-0282(199603)38:3<305::AID-BIP4>3.0.CO;2-Y.

Schneider-Poetsch, Tilman, et al. “Inhibition of Eukaryotic Translation Elongation by Cycloheximide and Lactimidomycin.” *Nature Chemical Biology*, vol. 6, no. 3, Mar. 2010, pp. 209–17. *DOI.org (Crossref)*, https://doi.org/10.1038/nchembio.304.

Sheppard, D. N., et al. “Mutations in CFTR Associated with Mild-Disease-Form Cl- Channels with Altered Pore Properties.” *Nature*, vol. 362, no. 6416, Mar. 1993, pp. 160–64. *PubMed*, https://doi.org/10.1038/362160a0.

Small-Molecule Drug Discovery Suite 2016–1. Maestro, version 10.5; LigPrep, version 3.7; Epik, version 3.5; Glide, version 7.0; Primer, version 4.3., Schrödinger LLC., 2016.

Spear, Eric D., and Davis T. W. Ng. “Stress Tolerance of Misfolded Carboxypeptidase Y Requires Maintenance of Protein Trafficking and Degradative Pathways.” *Molecular Biology of the Cell*, vol. 14, no. 7, July 2003, pp. 2756–67. *DOI.org (Crossref)*, https://doi.org/10.1091/mbc.e02-11-0717.

Spiess, Martin, et al. “Membrane Protein Integration and Topogenesis at the ER.” *The Protein Journal*, vol. 38, no. 3, June 2019, pp. 306–16. *DOI.org (Crossref)*, https://doi.org/10.1007/s10930-019-09827-6.

Stirling, C. J., et al. “Protein Translocation Mutants Defective in the Insertion of Integral Membrane Proteins into the Endoplasmic Reticulum.” *Molecular Biology of the Cell*, vol. 3, no. 2, Feb. 1992, pp. 129–42. *DOI.org (Crossref)*, https://doi.org/10.1091/mbc.3.2.129.

Sukharev, Sergei I., et al. “Energetic and Spatial Parameters for Gating of the Bacterial Large Conductance Mechanosensitive Channel, MscL.” *The Journal of General Physiology*, vol. 113, no. 4, Apr. 1999, pp. 525–40. *DOI.org (Crossref)*, https://doi.org/10.1085/jgp.113.4.525.

Sun, Zhihao, and Jeffrey L. Brodsky. “The Degradation Pathway of a Model Misfolded Protein Is Determined by Aggregation Propensity.” *Molecular Biology of the Cell*, edited by Benjamin S. Glick, vol. 29, no. 12, June 2018, pp. 1422–34. *DOI.org (Crossref)*, https://doi.org/10.1091/mbc.E18-02-0117.

Tector, M., and F. U. Hartl. “An Unstable Transmembrane Segment in the Cystic Fibrosis Transmembrane Conductance Regulator.” *The EMBO Journal*, vol. 18, no. 22, Nov. 1999, pp. 6290–98. *PubMed*, https://doi.org/10.1093/emboj/18.22.6290.

Vembar, Shruthi S., and Jeffrey L. Brodsky. “One Step at a Time: Endoplasmic Reticulum-Associated Degradation.” *Nature Reviews Molecular Cell Biology*, vol. 9, no. 12, Dec. 2008, pp. 944–57. *DOI.org (Crossref)*, https://doi.org/10.1038/nrm2546.

Virtanen, Pauli, et al. “SciPy 1.0: Fundamental Algorithms for Scientific Computing in Python.” *Nature Methods*, vol. 17, no. 3, Mar. 2020, pp. 261–72. *DOI.org (Crossref)*, https://doi.org/10.1038/s41592-019-0686-2.

Wang, Yang, et al. “The Push-to-Open Mechanism of the Tethered Mechanosensitive Ion Channel NompC.” *ELife*, vol. 10, June 2021, p. e58388. *DOI.org (Crossref)*, https://doi.org/10.7554/eLife.58388.

Watnick, T., et al. “Mutations of PKD1 in ADPKD2 Cysts Suggest a Pathogenic Effect of Trans-Heterozygous Mutations.” *Nature Genetics*, vol. 25, no. 2, June 2000, pp. 143–44. *PubMed*, https://doi.org/10.1038/75981.

White, Stephen H., and William C. Wimley. “Peptides in Lipid Bilayers: Structural and Thermodynamic Basis for Partitioning and Folding.” *Current Opinion in Structural Biology*, vol. 4, no. 1, Jan. 1994, pp. 79–86. *DOI.org (Crossref)*, https://doi.org/10.1016/S0959-440X(94)90063-9.

Whitley, Paul, et al. “A Nascent Secretory Protein 5 Traverse the Ribosome/Endoplasmic Reticulum Translocase Complex as an Extended Chain.” *Journal of Biological Chemistry*, vol. 271, no. 11, Mar. 1996, pp. 6241–44. *DOI.org (Crossref)*, https://doi.org/10.1074/jbc.271.11.6241.

Wiggins, Paul, and Rob Phillips. “Analytic Models for Mechanotransduction: Gating a Mechanosensitive Channel.” *Proceedings of the National Academy of Sciences*, vol. 101, no. 12, Mar. 2004, pp. 4071–76. *DOI.org (Crossref)*, https://doi.org/10.1073/pnas.0307804101.

Wimley, William C., and Stephen H. White. “Experimentally Determined Hydrophobicity Scale for Proteins at Membrane Interfaces.” *Nature Structural Biology*, vol. 3, no. 10, Oct. 1996, p. 842. *www.nature.com*, https://doi.org/10.1038/nsb1096-842.

Yang, Xuzhong, et al. “Structure Deformation and Curvature Sensing of PIEZO1 in Lipid Membranes.” *Nature*, vol. 604, no. 7905, Apr. 2022, pp. 377–83. *DOI.org (Crossref)*, https://doi.org/10.1038/s41586-022-04574-8.

Zhang, Liyan, et al. “Contribution of Hydrophobic and Electrostatic Interactions to the Membrane Integration of the Shaker K+ Channel Voltage Sensor Domain.” *Proceedings of the National Academy of Sciences*, vol. 104, no. 20, May 2007, pp. 8263–68. *DOI.org (Crossref)*, https://doi.org/10.1073/pnas.0611007104.

Zhang, Yixiao, et al. “Visualization of the Mechanosensitive Ion Channel MscS under Membrane Tension.” *Nature*, vol. 590, no. 7846, Feb. 2021, pp. 509–14. *DOI.org (Crossref)*, https://doi.org/10.1038/s41586-021-03196-w.

Zhu, Chongqin, et al. “Characterizing Hydrophobicity of Amino Acid Side Chains in a Protein Environment via Measuring Contact Angle of a Water Nanodroplet on Planar Peptide Network.” *Proceedings of the National Academy of Sciences*, vol. 113, no. 46, Nov. 2016, pp. 12946–51. *DOI.org (Crossref)*, https://doi.org/10.1073/pnas.1616138113.

Publishing Agreement

It is the policy of the University to encourage open access and broad distribution of all theses, dissertations, and manuscripts. The Graduate Division will facilitate the distribution of UCSF theses, dissertations, and manuscripts to the UCSF Library for open access and distribution. UCSF will make such theses, dissertations, and manuscripts accessible to the public and will take reasonable steps to preserve these works in perpetuity.

I hereby grant the non-exclusive, perpetual right to The Regents of the University of California to reproduce, publicly display, distribute, preserve, and publish copies of my thesis, dissertation, or manuscript in any form or media, now existing or later derived, including access online for teaching, research, and public service purposes.

DocuSigned by:
Yessica Gomez
9347286AF4CB4A1...
Author Signature

8/30/2023
Date